INTERNATIONAL JOURNAL OF CLIMATOLOGY
RMetS Royal Meteorological Society

MONTHLY RAIN AMOUNTS AT FABRA OBSERVATORY (BARCELONA, NE SPAIN): FRACTAL STRUCTURE, AUTOREGRESSIVE PROCESSES AND CORRELATION WITH MONTHLY WESTERN MEDITERRANEAN OSCILLATION INDEX

Journal:	*International Journal of Climatology*
Manuscript ID	JOC-15-0774.R1
Wiley - Manuscript type:	Research Article
Date Submitted by the Author:	25-Feb-2016
Complete List of Authors:	Lana, Xavier; Univ. Politècnica de Catalunya, Física i Enginyeria Nuclear Burgueño, August; Universitat de Barcelona, Astronomy and Meteorology serra, carina; Universitat Politècnica de Catalunya, Fisica i Enginyeria Nuclear Martinez, M. Dolors; Univ. Politècnica Catalunya, Fisica Aplicada
Keywords:	Monthly rain amount, Fractal structure, Autoregressive process, Western Mediterranean oscillation

MONTHLY RAIN AMOUNTS AT FABRA OBSERVATORY (BARCELONA, NE SPAIN): FRACTAL STRUCTURE, AUTOREGRESSIVE PROCESSES AND CORRELATION WITH MONTHLY WESTERN MEDITERRANEAN OSCILLATION INDEX

[(1)] Lana, X., [(2)] Burgueño, A., [(3)], Martínez, M.D. [(1)] Serra, C.

[(1)] Departament de Física i Enginyeria Nuclear. Universitat Politècnica de Catalunya.

[(2)] Departament d'Astronomia i Meteorologia. Universitat de Barcelona.

[(3)] Departament de Física Aplicada. Universitat Politècnica de Catalunya.

Running Title: Fractality and autoregressive processes of monthly rain amounts

Corresponding autor: Xavier Lana
francisco.javier.lana@upc.edu

ABSTRACT

Monthly rain amounts, MRA, recorded at Fabra Observatory (Barcelona, NE Spain) since 1917 to 2010, are analysed from two complementary points of view. First, mono- and multifractal characteristics of MRA are compared with those corresponding to the monthly Western Mediterranean Oscillation index, WeMOi, which affects the rainfall regime at the western Mediterranean region. Monofractality is analysed through Hurst and Haursdoff exponents, and a power law describing the dependence of MRA power spectra on frequency. The reconstruction theorem permits to quantify the complexity of the physical process by means of the correlation dimension and the Kolmogorov entropy. In agreement with this theorem, the predictive instability is also evaluated through the Lyapunov exponents. The multifractality is characterised by the critical Hölder exponent, as well as by the asymmetry and spectral width of the multifractal spectrum. And second, three predictive processes for MRA are tested. One of them is based on the assumption that MRA could be simulated by fractional Gaussian noise. The other two are, by one hand, an ARIMA(p,1,0) process for MRA; on the other hand, an adaptation of the ARIMA process for MRA taking as arguments preceding WeMOi. Finally, relationships between MRA and WeMOi confirm that outstanding MRA use to be coincident with negative WeMOi. An explanation is also proposed for the non negligible number of MRA corresponding to positive WeMOi.

KEYWORDS:

Monthly rain, Western Mediterranean Oscillation, mono- and multifractal analyses, autoregressive process, Fabra Observatory (Barcelona).

1. INTRODUCTION

Along last two decades, the pluviometric regime at the Fabra Observatory (Barcelona, NE Spain) has been analysed at local scale as also at regional and European scales, including different points of view as statistical distributions of daily, monthly and annual amounts (Burgueño et al., 2004; 2005, 2010), characterization of Standardised Precipitation Index (Lana et al., 2001), periodicities, irregularities and time trends of several pluviometric parameters (Lana et al., 2005; Martínez et al., 2007a; De Luis et al., 2009; González-Hidalgo et al., 2009; Gallego et al., 2011), extreme daily amounts (Lana et al., 1995; Beguería et al., 2009), monthly rainfall shortage (Martínez et al., 2010, 2012) and dry spell lengths (Lana et al., 2006, 2008a, 2008b, 2012; Serra et al., 2006, 2013, 2014). The Fabra Observatory rainfall data has also taken part in fractal analyses of monthly rainfall amounts, MRA, and dry spell lengths for Iberian Peninsula and Europe by considering nonlinear processes, taking advantage of monofractal theory based on self-invariance, self-affine series and reconstruction theorem (Martínez et al., 2007b; Lana et al., 2010).

The Western Mediterranean Oscillation index, WeMOi, was proposed by Martín-Vide and López-Bustins (2006) to detect atmospheric circulation patterns related to rainfall shortage or excess affecting the Eastern Iberian Peninsula (Martín-Vide et al., 2008; López-Bustins et al., 2008; Gonzalez-Hidalgo et al., 2009; Ríos-Cornejo et al., 2015a), being also used in other regional climatic applications (Azorín-Molina and Lopez-Bustins, 2008; Sánchez-Lorenzo et al., 2009; Vicente-Serrano et al., 2009; Ouachani et al., 2013; El Kenawy et al., 2013; Beranová and Kyselý, 2015; Ríos-Cornejo et al., 2015b). Other atmospheric modes of low variability are also in play in this region, as the Mediterranean Oscillation, MO, which is an expression of the North Atlantic Oscillation, NAO, in the Western Mediterranean, except for the summer months (Palukitof, 2003; Dünkeloh and Jacobeit, 2003). The NAO by itself keeps a low influence in this region and it behaves independently to WeMO (Martín-Vide and López-Bustins, 2006; Ciarlò and Aquilina, 2015).

The fractal nature of the rainfall processes is an accepted behaviour and numerous related studies have been published during the last decades. It can be cited in chronological order Lovejoy and Mandelbrot (1985), Rodríguez-Iturbe et al. (1989), Olsson et al. (1993), Hubert et al. (1993), Tessier et al. (1996), Harris et al. (1996), Veneziano et al. (1996), Svensson et al. (1996), de Lima and Grasman (1999), Mazzarella (1999), Mazzarella and Tranfaglia (2000), Sivakumar (2001a, b), Sivakumar et al. (2001), Salas et al. (2005), García-Marín et al. (2008), de Lima and de Lima (2009), Valencia et al. (2010), Capecchi et al. (2012), Verrier et al. (2011), Yonghe et al. (2012, 2013), Gires et al. (2013), Ghanmi et al. (2013), Rodríguez et al. (2013) and Mandapaka and Qin (2015), among many others. These references include a set of concepts (multifractality, chaotic behaviour, time persistence, predictability, fractal dimension, universal multifractal model, scale-invariance) applied to a variety of topics as rain intensity, annual amounts, precipitation caused by convective storms, characterisation and comparison of different climates and design and improvement of rain-gauge networks.

One of the main objectives of the present analysis is the fractal characteristics of MRA and comparison of their mono- and specially multifractal results with those obtained for the WeMOi (Lana et al., 2015), taking advantage of the known correlation between MRA and WeMOi (Martín-Vide and López-Bustins, 2006). In particular, the multifractal detrended fluctuaction analysis (MF-DFA) allows a reliable characterization of multifractal non-stationary and stationary time series (Kantelhardt et al., 2002). The MF-DFA has been applied in many scientific fields such as, for example, biology (Dutta, 2010), human health (Shimizu, 2002), seismology (Ghosh et al., 2012) or climatology (Feng et al., 2009; Mali, 2014; Burgueño et al., 2014; Lana et al., 2015). A detailed description of steps for applying the MF-DFA method can be found in the last two references.

In addition, three predictive schemes of MRA are proposed and tested. The first is a simulation of MRA by means of fractional Gaussian noise, fGn (Mandelbrott and van Ness, 1968; Turcotte, 1997). The second is a classical ARIMA(p,1,0) process (Box and Jenkins, 1976; Asteriou and Hall, 2011) and the third is an adaptation of the ARIMA(p,1,0) process, taking previous WeMOi as arguments for the prediction of MRA. Both ARIMA forecasting types are also known as univariate and multivariate procedures respectively, being based on past observations or by taking observations on another variable (Chatfield, 1985). Indeed, ARIMA process is widely applied to model monthly precipitation series (Wang et al., 2014), as also other climatological time series as surface temperature (Triacca et al., 2014), surface pressure (Al-Awadhi and Jolliffe, 1998) and droughts (Pan Chun et al., 2013). The reason why a fGn simulation and ARIMA processes at monthly scale become important is the irregular rainfall regime in the North-Western Mediterranean, with quite frequent periods of consecutive monthly shortage (Serra et al., 2013, 2014).

The manuscript is structured as follows. Section 2 introduces briefly the main patterns of the MRA and WeMOi database. Section 3 describes the mono- and multifractal theory, introducing results concerning MRA and making comparison with previous WeMOi fractal analysis (Lana et al., 2015). It also includes a simulation of MRA in terms of fGn. The ARIMA(p,1,0) process is briefly described in Section 4 and the resulting predictions of MRA are compared when using previous MRA or WeMOi as arguments. The results, especially the improvements on the MRA prediction, are discussed in Section 5 and conclusions are summarised in Section 6.

2. DATABASE

2.1 MRA at Fabra Observatory

MRA consists on monthly amounts derived from daily rainfall recordings, without lack of data, at Fabra Observatory (41°25´N, 2°8´E, 413 m above sea level, located 7 km from the Mediterranean coast, with the city of Barcelona lying between it and the shoreline). That is, a continuous series of 1128 MRA since 1917 to 2010. The homogeneity of the MRA series was confirmed by the von Neumann ratio test and by using the filtering process proposed by Zurbenko (Lana et al., 2003). Figure 1a shows the annual rain amount time series, being remarkable their variability, ranging from a minimum close to 400 mm/year to peaks above 900 mm/year and achieving a maximum slightly exceeding 1100 mm/year. This series of annual amounts has an average of 617.7 mm/year, a standard deviation of 150.3 mm/year and a coefficient of variation of 24.3%. Figure 1b shows the seasonal rain amount time series. As expected for a North-Western Mediterranean regime (Capel, 2000; Barry and Chorley, 2003), autumn (October, November, December) represents the main contribution to total rain amounts, and a third degree polynomial fit patterns is quite similar to that shown in Figure 1a. In spring, rain amounts are spread in the largest number of rainy days along this season. In summer, rain amounts use to be accompanied by rainstorms and in winter they are of minor contribution to annuals amounts (Lana et al., 2003). Rainfall shortage in autumn and spring hardly ever are balanced by copious rainfall in winter and especially in summer. Seasons have MRA averages of 66.0 mm/month (autumn), 43.4 mm/month (winter), 48.7 mm/month (spring) and 47.8 mm/month (summer). The standard deviations are 62.1, 41.9, 37.4 and 46.6 mm/month respectively.

2.2 WeMOi

The WeMOi is defined as the difference between the normalized monthly barometric series at San Fernando (Spain) (36^0 17’ N, 06^0 07’ W) and at Padova (Italy) (45^0 24’ N, 11^0 52’ E), with respective average and standard deviation being derived from the 1961-1990 period. WeMOi was accurately compiled and its quality data verified by Martín-Vide and López-Bustins (2006). Recordings since 1856 up to 2013 are available at *http://www.ub.edu/gc/English/wemo.htm*.

In agreement with its definition, this atmospheric circulation index is expected to be strongly linked to Mediterranean climate patterns in contrast with others well known indices, as the monthly North Atlantic Oscillation index, NAOi, with Atlantic climate influences. Positive phases of WeMOi are characterised by Azores anticyclone enclosing the south-west Iberian quadrant and low pressures over the Liguria Gulf. Negative phases are usually linked to Central Europe anticyclones (north of the Italian Peninsula) and low pressures at the south-west of the Iberian Peninsula. Neutral phases use to be coincident with north-eastern and south-western advections or low-pressure gradients over the Western Mediterranean. Very illustrative examples of synoptic maps concerning these WeMOi phases can be found in Martín-Vide and López-Bustins (2006).

The main time patterns of the WeMOi are shown in Figures 2a and 2b. The whole recording period, month by month, and a 13-months moving window are characterised by a clear decreasing trend since the first decade of the 20th century up to present. This behaviour would be in agreement with time patterns shown by WeMOi corresponding to spring and summer seasons, also characterised by similar decreasing trends.

2.3 Basic MRA – WeMOi connections

It is worth mentioning that trends affecting WeMOi moving window results (Figures 2a and 2b) are not detected on annual and seasonal rain amounts. This fact would strongly suggest that, as expected in a complex physical system as the atmospheric dynamics, MRA at the Fabra Observatory would be only partially governed by the time evolution of WeMOi. Another property to be considered for comparison between both signals is their statistical distribution. While MRA are gamma distributed, with discrepancies between empiric and theoretical model within the Kolmogorov-Smirnov 95% confidence bands all along the MRA range (Lana and Burgueño, 2000a, b), the WeMOi are Gaussian distributed (Lana et al., 2015). Only minor discrepancies on the MRA fit to the gamma model, without exceeding the confidence bands, are observed for MRA below or equal to 10 mm/month.

From a qualitative point of view, a relationship between Fabra Observatory MRA and WeMOi can be established from different synoptic atmospheric situations. Fabra Observatory, faced to the Mediterranean coast, is relatively protected against northern advections by the orographic barrier of the Pyrenees. Additionally, the long tracks of fronts travelling from the Atlantic to the Mediterranean coast, crossing the Iberian Peninsula, usually mitigate the effects of western advections on the Fabra Observatory pluviometric regime. Conversely, due to the vicinity to the Mediterranean coast, it may receive copious rain episodes associated with eastern advections. By taking into account these orographic and atmospheric constraints, and in agreement with Serra (1994), Fernandez Mills et al. (1994) and Serra et al. (1996), three synoptic situations generating rainfall episodes in Fabra Observatory, and connected to WeMOi, could be identified:

a) Mediterranean advections. The most copious rainfall episodes are associated with Eastern, North-eastern and South-eastern advections. They are usually characterised by low pressure nucleus, usually centred between the Balearic Islands and the South of the Iberian Peninsula, accompanied by strong anticyclones in Central Europe. At higher levels of the atmosphere the presence of a trough is quite usual. Although episodes of copious rainfall are not very frequent, they may generate outstanding run-offs and floods, especially in autumn, being not discarded such kind of episodes in winter and spring. All these Mediterranean advections would be linked to negative WeMOi.

b) Frontal passages. The rainfall episodes associated with frontal passages crossing the Iberian Peninsula from West to East or from North-west to South-east are many times almost

negligible. The long track from the Atlantic Ocean minimizes the possibility of copious rainfall episodes when fronts arrive to the Mediterranean coast, except for a few cases of robust cold fronts. These synoptic situations, linked to western or south-western advections, correspond to almost null or positive WeMOi.

c) Anticyclone combined with eastern advection. When the Azores anticyclone is slightly shifted towards the North, a weak eastern advection may be generated, which sometimes leads to very low or negligible rain amounts. These atmospheric patterns are compatible with small negative WeMOi.

Other situations, implying significant rainfall but without strong dependence on WeMOi phases, may be also considered. Heating of soil may generate convective phenomena favouring the vertical development of stormy clouds. These stormy episodes are usually observed at the end of summer, when a trough or cold air appear in mid-troposphere, then generating cellular storms. The rainfall episodes from these storms are usually very intense and copious but they use to happen at local scale and to be short-lived. A wider revision on the weather types in the western Mediterranean basin as also on their trends can be found in Grimalt et al. (2013), which apply an objective weather-type classification according to the Jenkinson and Collison procedure along the 1948-2009 period.

3. MONOFRACTAL AND MULTIFRACTAL ANALYSES

3.1 Monofractal theory.

The first analysed fractal parameter of MRA is the Hurst exponent, *H* (Turcotte, 1997), which is defined as the exponent of the power law

$$\frac{R(\tau)}{S(\tau)} \propto \tau^{H} \quad (1)$$

being $R(\tau)$ the range of the different segments of length τ of the series and $S(\tau)$ the corresponding standard deviation. It should be remembered that H close to 0.5 would imply a strong randomness of the series. Conversely, H clearly lowering or exceeding 0.5 would suggest anti-persistence or persistence respectively. Figure 3a shows the evolution of the quotient $R(\tau)/S(\tau)$ with τ in log-log scales. The computed H value is close to 0.54, so pointing to a notable randomness, with a very good confidence level in agreement with the square regression coefficient, ρ^2. In other words, future MRA would weakly depend on previous values, this fact possibly leading to consider high order autoregressive processes to improve predictions on MRA.

The self-affine behaviour of a series can be verified according to different methodologies. In agreement with Turcotte (1997), a classic box-counting method can be applied to obtain the Hausdorff exponent, H_a. According to this strategy, two relevant questions have to be considered. First, the fractal anisotropy of the series. This property would imply that a certain property $g(x,y)$ in a two dimensional space is not statistically similar to $g(rx,ry)$, where *r* is a scale factor, but similar to $g(rx,r^{H_a}y)$. And second, the Hausdorff exponent is quantified as $H_a = 2 - D$, being *D* the fractal dimension derived from the box-counting process. Alternatively, the semivariogram $\gamma(\tau)$ of the series depends on the segment length τ (Malamud and Turcotte, 1999) as

$$\gamma(\tau) = \gamma_0 \tau^{2H_a} \quad (2)$$

In such a way that the evolution of $\gamma(\tau)$ with the different lengths τ on a log-log scale permits a straightforward evaluation of H_a. Figure 3b depicts the semivariogram leading to a value of H_a very close to zero ($H_a \approx 0.01$).

The reconstruction theorem (Diks, 1999) leads to obtain valuable parameters as the minimum number of nonlinear equations, μ, describing a physical mechanism, the embedding dimension, d_E, necessary to obtain an asymptotic value, μ^*, of the correlation dimension and the Kolmogorov entropy, κ, which is a measure of the loss of memory of the physical process along the time. All of them quantify the complexity of the physical mechanism governing the time series analysed. The reconstruction theorem process is based on the generation of a set of *m*-dimensional space vectors:

$$z(i) = \{x(i), x(i+1), \ldots, x(i+m-1),\}, \quad i = 1,\ldots,N \quad (3)$$

and on the definition of the correlation integral in terms of the Grassberger-Procaccia formulation (Grassberger and Procaccia, 1983a,b)

$$C(m,r) = \lim_{N\to\infty} \frac{1}{N^2} \sum_{i,j=1}^{N} H\{r - \|z(i) - z(j)\|\} \quad (4)$$

being *r* an Euclidean distance in the *m*-dimensional space and *H{.}* the Heaviside function. Additionally, it is assumed that

$$C(m,r) = A_m e^{-m\kappa} r^{\mu(m)} \quad (5,a)$$

with $\mu(m)$ the correlation dimension. After plotting the correlation integral (Equation 5,a) in terms of *r* on log-log scales, according to

$$log\{C(m,r)\} = log(A_m) - m\kappa + \mu(m)log(r) \quad (5,b)$$

the corresponding slope is $\mu(m)$ for every reconstruction dimension m. It has to be underlined two factors which have to be carefully revised, as they could make erroneous $\mu(m)$ estimation: the lacunarity (Turcotte, 1997) for small values of *r*, and the saturation of $C(m,r)$ for high values of *r*, whatever the dimension m. An example for several reconstruction dimensions m is depicted in Figure 3c. The almost flat evolution of $C(m,r)$ for low values of *r,* as well as the saturation for high values of *r,* becomes quite evident. Increasing values of $\mu(m)$ are estimated for reconstruction dimensions arriving up to 20, tending these correlation dimensions towards an asymptotic value, μ^*, close to 7.2 (Figure 3d). This magnitude of μ^* is a first evaluation of the complexity of the signal: a minimum of seven nonlinear equations would be needed to describe the physical mechanisms governing the time series of MRA. The random component of MRA is also manifested by the high reconstruction dimension, m = 19 or 20, necessary to obtain asymptotic values of the correlation dimension. This required reconstruction dimension is also known as embedding dimension, d_E, of the analysed series.

Another relevant feature of the reconstruction theorem is the quantification of the loss of memory of the physical system. Prediction of accurate future MRA will be difficult if the Kolmogorov entropy, κ, is high. According to Equation (5,b), by naming the term $\log\{C(m,r)\} - \mu(m)\log(r)$ as $\alpha(m)$, we obtain

$$\alpha(m) = \log(A_m) - m\kappa \quad (5,c)$$

Equation (5,c) permits to make an easy estimation of κ by a least square regression of empiric $\alpha(m)$ in terms of m, provided that $\log(A_m)$ is constant. This constraint is only achieved for m tending to ∞, for which it is exected that A_{m+1}/A_m tends to 1.0. This behaviour of $\alpha(m)$ is shown in Figure 4a where the Kolmogorov entropy is estimated by taking into account the linear evolution of $\alpha(m)$ for m ranging from 17 to 20. If lower dimensions m are included, linearity disappears. In agreement with this strategy, MRA would be characterised by a complex underlying mechanism submitted to a loss of memory quantified by κ close to 1.09.

The last relevant application of the reconstruction theorem is the quantification of the predictive instability of MRA. Taking advantage of *m*-dimensional vectors generated according Equation (3), in agreement with Wiggins (2003), the Lyapunov exponents, λ_j $(j = 1, 2, ..., m)$, can be computed according to the algorithms proposed by Eckmann et al. (1986) and Stoop and Meier (1988). Assuming that the addition of all the m Lyapunov exponents is positive, the trajectory in the *m*-dimensional space will consist on aperiodic orbits around a strange attractor with a Kaplan-Yorke dimension, D_{KY} (Kaplan and Yorke, 1979). This dimension is computed as

$$D_{KY} = \ell_0 + \frac{1}{\left|\lambda_{\ell_0+1}\right|}\sum_{j=1}^{\ell_0}\lambda_j \quad (6)$$

with ℓ_0 the maximum number of Lyapunov exponents in decreasing order accomplishing $\lambda_1 + \lambda_2 + ... + \lambda_{\ell_0} \geq 0$. Figure 4b shows the evolution of the two first Lyapunov exponents towards asymptotic values, after a high enough number of iterations of the above mentioned algorithms. It is worth mentioning that, in agreement with Figure 4b, a minimum of 500 iterations is required and that the reconstruction theorem has to be applied at least up to m = 14 or 15 to assure the numerical stability of Lyapunov exponents. Predictive instability is confirmed given that the first Lyapunov exponent is positive. Additionally, taking into account Equation (6), the above mentioned strange attractor is characterised by a fractal structure with D_{KY} equal to 13.10.

3.2 Multifractal spectrum.

3.2.1 Singularity spectrum

According to Kantelhardt et al. (2002), the singularity spectrum $f(\alpha)$ can be related to the generalized Hurst exponent, *h(q)*, of the *q* order fluctuation function, $F_q(s)$, via a Legendre transform

$$\alpha = h(q) + q\frac{d[h(q)]}{dq} \overset{Legendre}{\leftrightarrow} f(\alpha) = q\cdot[\alpha - h(q)] + 1 \quad (7)$$

where α is the singularity strength or Hölder exponent, while $f(\alpha)$ denotes the dimension of the subset of the series. The multifractal scaling exponent is

$$\tau(q) = qh(q) - 1 \quad (8)$$

α being expressed as

$$\alpha = \frac{d\tau(q)}{dq} \quad (9)$$

The characteristics of the singularity spectrum provide a new way of comparing signals, because $f(\alpha)$ describes the dimensions of subsets of the series characterized by the same singularity

strength α . Designing α_o as the singularity strength with maximum spectrum or simply critical Hölder exponent, a small value of α_o means that the underlying process “loses fine-structure"; that is, it becomes more regular in appearance; while a large value of α_o ensures larger complexity. In this sense, the Hurst exponent can be roughly related to the position of α_o (see for instance Burgueño et al., 2014). The shape of $f(\alpha)$ may be fitted to a quadratic function around the position α_o,

$$f(\alpha) = A(\alpha - \alpha_0)^2 + B(\alpha - \alpha_0) + C \quad (10)$$

where *C* is an additive constant theoretically equal to 1. Coefficient *B* indicates the asymmetry of the spectrum, being zero for a symmetric spectrum. A right-skewed spectrum, *B>0,* indicates relatively strongly weighted high fractal exponents (with “fine-structure"), while left-skewed shapes, *B<0*, point to lower ones (more regular or smooth looking). The width of the spectrum, which is defined as the width of α , can be obtained by extrapolating the fitted curve to zero. Width *W* is simply defined as

$$W = \alpha_1 - \alpha_2 \quad (11)$$

with $f(\alpha_1) = f(\alpha_2) = 0$, being α_1 larger than α_2, and the wider the range of the Hölder exponent, the stronger the multifractality. In other words, the wider the range of α , the “richer" is the process in structure. A signal with a high value of α_o, a wide range of fractal exponents and a right-skewed shape is more complex than one with the opposite characteristics (Shimizu et al., 2002). Consequently, the fine-structure of physical mechanisms governing a signal could be analyzed if complexity is high. On the contrary, if the complexity of a signal is low, only the smooth-structure of these mechanisms could be detected. For monofractal series, the width of the spectrum will be zero and *h*(*q*) will be independent of *q*. Hence, from Equation (7), it is clear that there would be a unique value of α and $f(\alpha)$, the value of α being the Hurst exponent *H* and the value of $f(\alpha)$ being equal to 1.

3.2.2 MRA multifractal spectrum

The characteristics of the multifractal spectrum of MRA after applying the MF-DFA procedure for *q* ranging from −15 to +15 are shown in Figure 5a-5e. Figure 5a shows the *q*-order fluctuation function for *q* = ±15, where it can be observed that, in spite of some fluctuations, empiric values of $F_q(s)$ are fitted quite well to power laws with exponents given by generalised Hurst exponents *h(q).* The dependence of these exponents, as well as Hölder, α , and multifractal scaling exponents on *q*, $\tau(q)$, are depicted in Figures 5b-5d. Empirical values of $\tau(q)$ are well described by a second order polynomial on *q* and the Hölder exponent depends almost linearly on *q*, at least for the ±15 range considered. The empiric multifractal spectrum is shown in Figure 5e. As expected, the critical Hölder

exponent, α_0 = 0.52, would be in agreement with the Hurst exponent, *H* = 0.54, obtained from the rescaled analysis, being confirmed the notably randomness of MRA. Additionally, a non null spectral width of *W* = 0.44 confirms the multifractal structure of MRA and a negative asymmetry (*B* = −1.08) suggests that a "fine structure" of the physical process leading MRA should be difficult to determine.

3.3 Power spectrum and fractional Gaussian noise.

The power spectrum computation is a previous and necessary step to analyse a possible fGn behaviour of a time series (Turcotte ,1997; Malamud and Turcotte, 1999). MRA autocorrelation, $C(\tau)$, as a function of lag τ given in months, and its power spectrum, $S(f)$, are shown in Figures 6a and 6b. Autocorrelation is characterised by a narrow range (−0.1, +0.2) of low values and signs of an increasing tendency on $C(\tau)$ for lags approximately above 360 months. This fact would suggest that autoregressive processes would need for a long series of preceding monthly values to reasonably predict the next MRA. In agreement with the spectral contents depicted in Figure 6b, two clear periodicities are detected: one year and half a year, the rest of periods remaining with low spectral amplitude. When comparing WeMOi periodicities (Lana et al., 2015) with those detected for MRA, only the one-year periodicity is coincident. Half a year periodicity does not appear in WeMOi and, conversely, 19.1 years periodicity for WeMOi is not found for MRA. Additionally, $S(f)$ has an almost null trend with frequency f, proportional to the power law $f^{-\beta}$, being β equal to +0.04, after estimation based on the algorithm proposed by Malamud and Turcotte (1999).

After determining empiric values of parameters H, H_a and β, MRA could be simulated by fGn (Turcotte, 1997). This hypothesis is based on the fact that fGn is compatible with Hausdorff exponents close to zero and β parameters within the ±1 range. Moreover, fGn is compatible with a Hurst exponent close to 0.5 and an almost null value of β (Turcotte, 1997). fGn may be then obtained after the following steps:

a) Generation of white Gaussian noise, wGn.
b) Discrete Fourier transform, DFT, of the wGn.
c) Application of the filter $\left\{\frac{m}{N-1}\right\}^{\beta/2}$ to the spectral compounds of the wGn, where *N* is the number of samples of the wGn and *m* the number of spectral frequencies.
d) Generation of fGn by applying the inverse Fourier transform to the filtered wGn.

The similarity between MRA and fGn is quantified in terms of the mean absolute deviation, MAD (Stephenson et al. 2000),

$$MAD = \frac{1.483}{N}\sum_{j=1}^{N}\left|MRA(j) - s(j)\right| \quad (12)$$

where MRA(j) is the empiric amount for month j, s(j) the corresponding simulated value and *N* the number of elements of the series. If MAD is less than or equal to one standard deviation of MRA, the simulated fGn of the empiric series could be assumed as right. Obviously, this possibility does not mean that the simulated series is necessarily a good month by month prediction of MRA. It would be only established that the self-affine character, persistence or randomness and power spectral contents are similar. Figure 6c depicts the first 500 empiric MRA compared with a sample of fGn. According to the value of MAD (61.6 mm/month) and the standard deviation of MRA (48.4 mm/month), it has to be assumed that the fGn is only a rough approach to the empiric MRA. Additionally, fGn exceeding 150 mm/month (dashed line in the plot) are not generated. Then, about 4% of the data sample is not reproduced by the fGn. Though this percentage is low, a notable shortcoming of fGn is that copious MRA are not simulated. Autoregressive processes, developed in the forthcoming section, become necessary to improve MRA prediction.

4. AUTOREGRESSIVE PROCESS

The autoregressive integrated moving average ARIMA(p,d,0) model (Box and Jenkins, 1976) assumes that

$$\Delta^d x(i) = \theta + \mu\, x(i-1) + \sum_{k=1}^{p} \delta_k \Delta^d x(i-k) + a_i \quad (i = p+2, \ldots, N) \tag{13a}$$

where $\{x\}$ is a set of N empirical data and Δx is the set of first differences $\Delta x(i) = [x(i+1) - x(i)]$ and $\Delta^d x(i-k) = [x(i-k+1) - x(i-k)]^d$. $\{\theta, \mu, \delta_1, \ldots, \delta_p\}$ are the parameters of the autoregressive process, $\{a\}$ is a noise series and d is a real number. Alternatively, the ARIMA(p,d,0) model, with d = 1.0, can be written as

$$x(i) = \theta + \sum_{k=1}^{p} \delta_k x(i-k) + a_i \quad , i = p+1, \ldots, N \tag{13b}$$

where the time series $\{x\}$ is directly used instead of first differences. With the aim of avoiding singularities in the linear system of equations used to estimate $\{\theta, \mu, \delta_1, \ldots, \delta_p\}$, parameter μ is implicitly included in parameter δ_1. Equation (13b) is usually designed as autoregressive process of order p, AR(p). The resulting system of linear equations, disregarding the stochastic component $\{a\}$, can be represented in terms of matrix formulation as

$$Z = A\,W \tag{14a}$$

with *Z* the $\{x(p+1), x(p+2), \ldots, x(n)\}$ vector, *n* the number of empiric elements belonging to series $\{x\}$, and the (*n*-*p*-1, *p*+1) matrix *A* multiplying a *p*+1 dimension vector *W* containing the parameters $\{\theta, \mu, \delta_1, \ldots, \delta_p\}$ to be solved from Equation (14a). The components of vector *W* can be estimated by multiplying Equation (14a) by the transposed *A* matrix, A^T

$$A^T Z = A^T A\, W \tag{14b}$$

Remembering that the symmetric matrix $A^T A$ can be decomposed in two triangular matrices, it is straightforward to obtain the values of parameters $\{\theta, \delta_1, \ldots, \delta_p\}$ taking advantage of the Crout's algorithm (Press et al., 1992).

A convincing solution of Equation (13b) demands some criterion to decide the optimum autoregressive order, OAO. The decision can be taken by searching for the autoregressive order leading to a minimum of MAD (Equation 12).

4.1 Autoregressive process for MRA

The evolution of the MAD with the autoregressive order *p* is shown in Figure 7a. The reduction of the MAD is persistent with increasing order *p* but small, being finally chosen 145 as the *p* order with minimum MAD for *p* ranging from 2 to 150. Higher orders of *p* are not advisable given that computational instabilities appear when the above mentioned Crout's algorithm is applied to solve Equation 13b for autoregressive orders *p* above 200. Figure 7b shows the time series of the MRA

residuals, defined from the difference between a predicted MRA by the AR(p=145) and the corresponding empiric MRA. Positive (negative) residuals represent overestimation (underestimation) of MRA. Bearing in mind the standard deviation of the empiric MRA (σ_{MRA} = 48.4 mm/month) and of the residuals (σ_{res} = 45.1 mm/month), 76.7% of MRA residuals are included within the ($-\sigma_{res}$, $+\sigma_{res}$) interval. Extreme MRA residuals (out of $\pm 2.0\sigma_{res}$) represent a percentage of 3.7%. These last MRA residuals should be assumed as due to MRA predictions with excessive errors. The MRA residuals are distributed asymmetrically, without any value below $-2.0\sigma_{res}$ (Figure 7c). Although the MRA residuals are mostly distributed within the ($-\sigma_{res}$, $+\sigma_{res}$) interval (±45.0 mm/month), positive residuals (overestimations) are a bit more numerous than negative residuals (underestimation), in such a way that MRA residuals are not Gaussian distributed, as the Kolmogorov-Smirnov test (Press et al, 1992) at 95% confidence level proofs. In spite of this, relevant biases on MRA estimations are not expected because the average of the MRA residuals is close to −1.0 mm/month.

4.2 Regressive process for MRA depending on previous WeMOi

A different strategy to search for reasonable predictions of MRA consists on adapting the AR(p) process changing the argument *x(i-k) = MRA(i-k)* by *x(i-k) = WeMOi (i-k)* in Equation (13b)

$$MRA(i) = \theta + \sum_{k=1}^{p} \delta_k WeMOi(i-k) + a_i \quad , i = p+1, ..., N \tag{15}$$

Then, the assumed hypothesis is that a MRA depends on preceding WeMOi. Figure 8a depicts the evolution of the respective MAD with the autoregressive order *p* up to 200, being finally chosen the OAO as 180. Similarly to the previous autoregressive process, the evolution of MAD tends to be monotonically decreasing, achieving a minimum close to 46.0 mm/month, slightly lower than that detected for the first autoregressive process. For this selected 180 order, σ_{res} = 40.4 mm/month and 74.9% of residuals keep inside the ($-\sigma_{res}$, $+\sigma_{res}$) interval (Figure 8b). Extreme MRA residuals out of the $\pm 2.0\sigma_{res}$ range represent a percentage of 3.5%. These last MRA residuals should be assumed again as due to MRA predictions with excessive errors. According to Figure 8c, the asymmetry of the MRA residuals is quite clear and once again they are not Gaussian distributed. Consequently, the regressive process based on the dependence of MRA on WeMOi would only represent small improvements on the MAD (a slightly better global fit) and a reduction of extreme discrepancies between real and predicted MRA (from close to 280.0 mm/month to 240.0 mm/month). Additional information can be obtained by searching for some relationship between MRA residuals and positive and negative WeMOi. Figure 8d shows a great percentage of MRA residuals within the ±100.0 mm/month range corresponding to WeMOi ranging from −4.0 to +1.0 (mainly negative WeMOi), while a low percentage of MRA residuals is associated with WeMOi ranging from +1.0 to +4.0. It is also worth mentioning that all MRA residuals exceeding 110.0 mm/month correspond to WeMOi within the (−4.0, 1.0) range.

The relationship between MRA and WeMOi can be also characterised by means of their cross-correlation and their cross-power spectrum. Figure 9a shows the cross-correlations at seasonal scale. The four curves of cross-correlation depict a common pattern, which consists on small positive coefficients for the first lags and a tendency to negative coefficients for longer lags. This behaviour is especially evident for spring (April, May, June) and summer (July, August, September). Spring season is characterised by notable cross-correlation coefficients lower than −0.8 for lags larger than or equal to 60 seasons**.** Remembering that every season is made up by three months, negative correlations between MRA and WeMOi would be expected after a lag of, at least, 180 months. Summer season depicts quite similar patterns. Nevertheless, negative correlation coefficients lower than −0.8 are detected for lags close to 110 seasons, equivalent to an elapsed time of 330 months. Winter (January, February and March) and autumn (October, November and December) seasons are not characterised by a clear decreasing tendency of the cross-correlation coefficients. Notable negative cross-correlations are detected in winter for lags equal to 35 (105 months) and 115 (345 months). Autumn also depicts relevant negative cross-correlations for five lags from 50 (150 months) to 120 (360 months). Figure 9b describes the evolution of the cross-correlation coefficients at monthly scale. The similarities of monthly and summer and spring cross-correlations are quite evident. The cross-power spectrum for monthly series is shown in Figure 9c. Besides the expected periodicities of one year and half a year, other relevant periodicities have not been found.

An additional description of possible relationships between MRA and WeMOi are shown in Figure 10. A high percentage of MRA below 100.0 mm/month corresponds to WeMOi within the (−4, +1) interval. Above 100.0 mm/month, a high number of MRA correspond to the same (−4, +1) interval, and even some MRA with values within the (200.0 - 300.0 mm/month) range correspond to positive WeMOi ranging from 0 to +1. In short, notable MRA would not be always assigned to negative WeMOi.

5. DISCUSSION OF THE RESULTS.

5.1 Comparison of mono and multifractal results.

Although fractal parameters are not absolutely coincident, MRA and WeMOi fractals results (Table 1) are characterised by some coincidences, both signals keeping a remarkable complexity. First of all, it is worth mentioning that both series could be assimilated to fGn according to their Hurst and Hausdorff exponents and their β parameters. MRA also manifest a notable randomness in agreement with its Hurst exponent, as well as clear signs of an uncorrelated stationary behaviour according to its β parameter, close to zero. On the contrary, WeMOi depicts some signs of persistence. This fact would be in agreement with the Kolmogorov entropy, which suggests a stronger loss of memory of the physical process governing MRA in comparison with that associated with WeMOi. The complexity of the physical mechanisms, which can be quantified by the minimum number of nonlinear equations, μ^*, governing them, is slightly higher for the WeMOi than for MRA. Nevertheless, the predictive instability, given basically by the first Lyapunov exponent, λ_1, is coincident for both series. Two other common features concerning the Lyapunov exponents have to be mentioned. First, the sum of all Lyapunov exponents is negative for both series. Therefore, the trajectories of both physical systems in the *m*-dimensional space will not collapse towards a fixed point neither diverge to infinite, but these trajectories consist on aperiodic orbits around a fractal structure, known as a strange attractor with a fractal dimension less than *m*. This fractal dimension, also known as Kaplan-Yorke, D_{KY}, dimension, is very similar for both series. Consequently, the predictive instability and the chaotic behaviours of both series are quite similar.

With respect to the multifractal behaviour of both series, it has to be mentioned the very close critical Hölder exponents obtained for MRA and WeMOi. Bearing in mind the linear relationship between α_0 and the Hurst exponent (Burgueño et al., 2014), this similarity would agree with the close Hurst exponents derived from rescaled analysis. Additionally, according to Equation (15), both multifractal spectra are centred on similar α_0. Nevertheless, their spectral width, *W*, and asymmetry, *B*, disagree. Remembering that *W* quantifies the degree of multifractality (*W* equal to zero would imply a pure monofractal structure), MRA depicts a larger multifractal structure than WeMOi. Bearing in mind the meaning of the asymmetry, whereas the fine-structure of WeMOi could be analysed ($B > 0$), a not so detailed picture of MRA could be obtained due to its negative *B* parameter.

5.2 Fractional Gaussian noise simulation and autoregressive processes for MRA

In agreement with results obtained from the reconstruction theorem and parameters of the multifractal spectrum, it has to be accepted the prediction of MRA as complex, similarly to the WeMOi (Lana et al., 2015). By comparing the obtained values of MAD and the standard deviation of MRA, fGn are just simulation series reproducing mean, standard deviation, Hurst and Hausdorff

exponents and the β exponent of the power law related to the power spectrum. Shortcomings of prediction based on fGn become evident in Figure 6c. First, a single time shift to match MRA and fGn is difficult to be obtained. And second, MRA above 150.0 mm/month are not generated by the fGn.

An alternative to the fGn simulation could be an ARIMA(p,1,0) process. In spite of a number of shortcomings (the number of non-linear equations suggested by the correlation dimension, the loss of memory associated with the Kolmogorov entropy, the Hurst exponent suggesting randomness and the predictive instability manifested by the Lyapunov exponents), the AR(p) process permits some improvements, basically a reduction of its MAD in comparison with the standard deviation of MRA. It is also worth mentioning that 13% (10.3%) of MRA are underestimated (overestimated) by amounts exceeding 50.0 mm/month. Additionally, all overestimations (ranging from 0 to 70.0 mm/month) are much more moderate than underestimations, which range from 0 to 280.0 mm/month. Consequently, the shortcoming of the AR(p) algorithm would be the underestimation of some MRA.

A question which could be in some way surprising is the high number *p* of preceding MRA required to predict the *p*+1 value. This situation could be consequence of several factors such as autocorrelation coefficients within the ±0.1 range and with only some signs of increasing values (Figure 6a) for lags exceeding 300 months. Also, the high OAO could be due to the above mentioned loss of memory of the physical mechanisms (not null Kolmogorov entropy) and a Hurst exponent suggesting randomness. The evolution of MAD with the auto-regression order *p* could be approximated by two decreasing linear trends (Figure 7a), with a change of slope for *p* close to 60. In agreement with this Figure, notable improvements on MAD should not be expected for *p* exceeding 150. Additionally, the above mentioned computational instabilities when solving Equation 13b for *p* exceeding 200 should be taken into consideration. As a summary, in agreement with Table 2, the prediction of MRA in terms of previous WeMOi is characterised by the lowest MAD, with the lowest ratio $\sigma_{res}/\sigma_{MRA}$ among the three predictive processes. Although the MRA residuals are not small, improvements on predictability with respect to fGn simulations and the AR(p) process are quite evident.

5.3 Dependence of MRA on preceding WeMOi.

A first approach to the dependence of MRA on preceding WeMOi would be based on the assignment of rainfall episodes to negative WeMOi, in agreement with synoptic situations leading to rainfall in the Western Mediterranean coast (see Section 2). This hypothesis would be relatively confirmed by taking into account cross-correlations at seasonal and monthly scales (Figures 9a and 9b), where negative coefficients are quite usual. Nevertheless, the relationship between MRA and preceding WeMOi is a bit more complex. First of all, cross-power spectrum (Figure 9c) only clearly depicts two expected periodicities (one year and half a year), which do not contribute relevantly to a description of the relationship between both series. And second, the regression process based on the assumed dependence of MRA on preceding WeMOi depicts similar results to that obtained for the AR(p)

algorithm. These are: a high value of *p* is needed again, the OAO being similar to that obtained for the AR(p) process. The percentages of MRA residuals below or above ±σ and ±2σ are also similar and predictions are once again unbiased (the expected value of the MRA residuals is very close to zero). Nevertheless, a difference has to be mentioned: the vicinity to a Gaussian distribution of MRA residuals is closer than that obtained from the AR(p) process. Additionally, as Figure 8d depicts, the quite complex relationship between MRA residuals and WeMOi can be summarized after the regression process. A high ratio of MRA residuals, mostly lowering 80.0 mm/month, are associated with WeMOi within the (−4.0, +1.0) range. Conversely, a short number of residuals mostly below 80.0 mm/month correspond to WeMOi larger than or equal to +1.0

Another point of view of the complex relationship between MRA and WeMOi is shown in Figures 10a. In spite of numerous examples with MRA linked to negative WeMOi, a non negligible number of MRA below 200.0 mm/month corresponds to positive WeMOi and only amounts exceeding this threshold are restricted to WeMOi within the (-4, +1) range. These facts would not be completely explained by a simple relationship between high MRA and negative WeMOi. A quite similar distribution can be observed at seasonal scale (Figures 10b), especially in autumn, season for which MRA above 200.0 mm/month are a bit more frequent than in the rest of seasons, very likely due to the contribution of eastern advections. The monthly scale of the analysis would be a possible explanation to this lack of a clear expected relationship between high MRA and negative WeMOi. Synoptic situations generating rainfall episodes may change in a few days, in such a way that MRA might result from events with different meteorological conditions. This fact does not necessarily imply a negative WeMOi, which is deduced from the summary of daily barometric records in two different meteorological stations along a month. An example could be a month with persistent high pressures (anticyclonic situation), interrupted by a few days with eastern advection accompanied by copious rainfall. The result would be a notable MRA and, possibly, a moderate positive WeMOi. It is also worth mentioning that seasonal averages of MRA (mm/month) and WeMOi are 48.7 and 0.39 (spring), 47.8 and 0.22 (summer), 66.0 and -0.01 (autumn) and 43.4 and 0.03 (winter) respectively. According to these quantities, winter and especially autumn would be the seasons with more concordance between MRA and negative WeMOi. Conversely, this concordance would be more debatable for spring and summer.

The significance of the daily WeMO index on the monthly index, WeMOi, and its impact on outstanding MRA may be derived from three selected months (Table 3). October 1965 is characterised by the most negative WeMOi (-3.21) of the series. This is a month with a notable number of rainy days and negative daily WeMO indices. It keeps very similar expected and standard deviation of daily amounts, suggesting persistent synoptic situations in agreement with negative WeMOi. A revision of daily synoptic surface charts (www.netweather.tv) shows a quite persistent low pressure at the SW or W of the Iberian Peninsula and a Central Europe anticyclone. This synoptic

situation generates E or SE advection on the NE Spain, leading to heavy and persistent rainfall in Fabra Observatory. This is an example for which high MRA and negative WeMOi would be in almost perfect concordance.

December 1971 (Table 3) is characterised by a moderate negative WeMOi and a high number of high pressure days on the Iberian Peninsula (almost null or positive daily WeMO index). Nevertheless, a few days at the beginning and at the end of the month had negative WeMO index, with a low at the south of the Iberian Peninsula and a high centred on British Islands. This synoptic situation led to copious rainfall at the Fabra Observatory due to eastern advection. For instance, 196 mm/month were recorded on December 8th, 1971.

September 1993 (Table 3) corresponds to a positive WeMOi and a remarkable MRA of 248.1 mm/month. A close revision of daily WeMO indices manifests that only six days had negative WeMO index. The analysis of synoptic surface and 500 hPa charts shows that rainy days are not linked to a particular daily WeMO index sign. At surface level, the main pattern is an almost null pressure gradient over the Iberian Peninsula, whereas 500 hPa charts manifest the presence of a through. This through, combined with a relative low pressure in the Mediterranean coast, produced intense convective precipitation of short life, quite common at the end of summer. It is outstanding the maximum daily amount recorded on September 30th at Fabra Observatory (90.9 mm/month). It is worth of mention that all these three synoptic situations leading to notable daily amounts, whatever the sign of WeMOi, are in agreement with clusters obtained by Martín-Vide et al. (2008**).**

Discrepancies at monthly scale between MRA and WeMOi could be also consequence of other factors. The Fabra Observatory pluviometric regime is governed by a complex dynamic atmospheric mechanism, which could be sometimes clearly linked to WeMO index, but without neglecting the influences of other indices such as the NAO, MO and Artic Oscillation, AO, among others (Gonzalez-Hidalgo et al., 2009; Ríos-Cornejo et al., 2015). Additionally, the geopotential height for 500 hPa, characteristic not considered by these circulation indices, could be another relevant factor governing some rainfall episodes, especially at the end of summer and in autumn.

A complementary point of view of these facts is shown in Figures 11a and b. The ratio of positive WeMOi related to different MRA is shown in Figure 11a. It is worth mentioning that this ratio exceeds 50% up to 80 mm/month, it fluctuates around this percentage up to 140 mm/month and clearly it decreases to 10-20% for MRA exceeding 140 mm/month. Consequently, even for the highest MRA, a non-negligible number of MRA are linked to positive WeMOi. Quite similar patterns are detected for the evolution of the average WeMOi, <WeMO>, shown in Figure 11b. Whereas <WeMO> fluctuates around zero for MRA from 80 to 140 mm/month, it becomes clearly negative for MRA exceeding 140 mm/month.

6. CONCLUSIONS.

A detailed analysis of the mono- and multifractal properties of MRA recorded at the Fabra Observatory (Barcelona, Spain) has permitted to ascertain the complexity of the physical mechanisms and the predictive instabilities of this rainfall series. All these properties have been compared with those corresponding to the WeMOi. In concordance with the meaning of the multifractal parameters, a fine structure of WeMOi should be easier determined than for MRA.

The prediction of MRA has been attempted from three points of view: fGn, ARIMA(p,1,0) on preceding MRA and ARIMA(p,1,0) on preceding WeMOi. Results of the fGn simulation are improved by both ARIMA regressive processes, which obtain a better match between real and predicted MRA, with MAD smaller than those obtained for the fGn model and with a reduction of the standard deviations of the MRA residuals. In short, the best predictive regression would be that based on the dependence of MRA on previous WeMOi.

The hypothesis of a relationship between MRA and negative WeMOi has been valuated taking into account MRA-WeMOi cross-correlations and diagrams representing relationships between different MRA ranges and WeMOi. Both evaluation techniques are not conclusive with respect to the proposed hypothesis. Negative cross-correlations are not very relevant. Additionally, some notable MRA and a non negligible number of moderate MRA are associated with positive WeMOi. As proposed in Section 5, this behaviour should be the consequence of series being evaluated at monthly scale but including rain episodes only a few days long. Shorter recording time scales could be then convenient to establish a more clear relationship between rain amounts and WeMOi. Additionally, as mentioned in Section 5.3, other indices based on atmospheric pressure at sea level, sea surface temperature or geopotential height at 500 hPa should not be discarded as factors conditioning recorded MRA series.

ACKNOWLEDGMENTS

The *Reial Acadèmia de Ciències i Arts de Barcelona* kindly provided the time series of daily rainfall amounts of Fabra Observatory. The authors would also thank to the anonymous reviewers their comments and suggestions.

References

Al-Awadhi S., Jolliffe I. (1998): Time series modelling of surface pressure data. Int. J. Climatol. 18,443–455.

Asteriou D., Hall, S. G. (2011). ARIMA models and the Box–Jenkins methodology. Applied Econometrics (Second ed.). Palgrave MacMillan. pp. 265–286.

Azorin-Molina C., Lopez-Bustins J.L. (2008). An automated sea breeze selection technique based on regional sea-level pressure difference: WeMOi. Int. J. Climatol., 28, 1681-1692.

Barry R.G., Chorley R.J. (2003): Atmosphere, Weather and Climate. 8th edition. Routledge. London. 421 pp.

Beguería S., Vicente-Serrano S.M.,Juan I. López-Moreno J.I., García-Ruiz J.M. (2009): Annual and seasonal mapping of peak intensity, magnitude and duration of extreme precipitation events across a climatic gradient, northeast Spain. Int. J. Climatol., 29, 1759-1779. DOI: 10.1002/joc.1808

Beranová R., Kyselý J. (2015): Links between circulation indices and precipitation in the Mediterranean in an ensemble of regional climate models. Theor. Appl. Climatol., DOI 10.1007/s00704-015-1381-6

Box G.E.P., Jenkins G.M. (1976). Time Series Analysis: Forecasting and Control. Holden-Day, California, 575 pp.

Burgueño A., Serra C., Lana X. (2004). Monthly and annual statistical distributions of the daily rainfall at the Fabra Observatory (Barcelona, NE Spain) for the years 1917-1999. Theor. Appl. Climatol., 77, 57-75.

Burgueño A., Martínez M.D., Lana X., Serra C. (2005). Statistical distributions of the daily rainfall regime in Catalonia (NE Spain) for the years 1950-2000. Int. J. Climatol., 25, 1381-1403.

Burgueño A., Martínez M.D., Serra C., Lana X. (2010). Statistical distributions of daily rainfall regime in Europe for the period 1951-2000. Theor. Appl. Climatol., 102, 213-226.

Burgueño A., Lana X., Serra C., Martínez M.D. (2014). Daily extreme temperature multifractals in Catalonia (NE Spain). Physics Letters A, 378, 874-885.

Capecchi V., Crisci A., Melani S., Morabito M., Politi P. (2012). Fractal characterization of rain-gauge networks and precipitations: an application in Central Italy. Theor. Appl. Climatol., 107, 541-546. DOI 10.1007/s00704-011-0503-z.

Capel J.J. (2000): El clima de la Península Ibérica. Ariel Geografía. Ariel. Barcelona. 281 pp.

Chatfield C. (1985). The analysis of time series: an introduction. Chapman and Hall. London, 286 pp.

Ciarlò J.M., Aquilina N.J. (2015). An analysis of teleconnections in the Mediterranean region using RegCM4. *Int. J. Climatol.,* DOI: 10.1002/joc.4383.

De Luis M, González-Hidalgo J.C., Longares L.A., Štepánek P. (2009) Seasonal precipitation trends in the Mediterranean Iberian Peninsula in second half of 20th century. *Int. J. Climatol.*, 29, 1312-1323.

Diks C. (1999). Nonlinear time series analysis. Methods and applications. In: Nonlinear time series and chaos, 4. World Scientific, London, 209 pp

Dutta S. (2010). EEG pattern of normal and epileptic rats: monofractal or multifractal? Fractals, 18, 425-431.

Dünkeloh A, Jacobeit J. (2003). Circulation dynamics of Mediterranean precipitation variability 1948–1998. *Int. J. Climatol.*, 23, 1843–1866.

Eckmann J. P., Oliffson S., Ruelle D., Cilliberto S. (1986). Lyapunov exponents from time series. Phys. Rev. A, 34(6), 4971–4979.

El Kenawy A., López-Moreno J.I., Vicente-Serrano S.M. (2013). Summer temperature extremes in northeastern Spain: spatial regionalization and links to atmospheric circulation (1960-2006). Theor. Appl. Climatol., 113, 387-405.

Feng T., Zuntao Fu Z., Deng X., Mao J. (2009): A brief description to different multi-fractal behaviors of daily wind speed records over China. Physics Letters A, 373, 4134–4141.

Fernández Mills G., Lana X., Serra C. (1994). Catalonian precipitation patterns: principal component analysis and automated regionalization. Theor. Appl. Climatol., 49, 201-212.

Gallego M.C., Trigo R. M., Vaquero J.M., Brunet M., García J.A., Sigró J., Valente M.A. (2011): Trends in frequency indices of daily precipitation over the Iberian Peninsula during the last century. J. Geophys. Res., 116, D02109, doi:10.1029/2010JD014255.

García-Marín A.P., Jiménez-Hornero F. J., Ayuso-Muñoz J. L. (2008). Universal multifractal description of an hourly rainfall time series from a location in southern Spain. Atmósfera, 21, 347-355.

Ghanmi H., Bargaoui Z., Mallet C. (2013). Investigation of the fractal dimension of rainfall occurrence in a semi-arid Mediterranean climate. Hydrological Sciences Journal – Journal des Sciences Hydrologiques, 58 (3), 483-497.

Ghosh D., Dep A., Dutta S., Sengupta R., Samanta S. (2012). Multifractality of radon concentration fluctuation in earthquake related signal. Fractals, 20, 33-39.

Gires A., Tchiguirinskaia I., Schertzer D., Lovejoy S.(2013). Development and analysis of a simple model to represent the zero rainfall in a universal multifractal framework. Nonlin. Processes Geophys., 20, 343–356.

González-Hidalgo J.C., Lopez-Bustins J.A., Štepánek P., Martin-Vide J., de Luis M. (2009). Monthly precipitation trends on the Mediterranean fringe of the Iberian Peninsula during the second-half of the twentieth century (1951–2000). Int. J. Climatol., 29, 1415-1429.

Grassberger P., Procaccia I. (1983a). Characterization of strange attractors, Phys. Rev. Lett., 50, 346–349.

Grassberger P., Procaccia I. (1983b). Estimation of the Kolmogorov entropy from a chaotic signal, Phys. Rev. A, 28, 448-451.

Grimalt M, Tomás M, Alomar G, Martín-Vide J, Moreno-García MC (2013): Determination of the Jenkinson and Collison's weather types for the western Mediterranean basin over the 1948-2009 period.Temporal analysis. Atmósfera 26(1), 75-94.

Harris D., Menabde M., Seed A., Austin G. (1996). Multifractal characterization of rain fields with a strong orographic influence, J. Geophys. Res., 101, 26 405–26 414.

Hubert P., Tessier Y., Lovejoy S., Shertzer D., Schmitt F., Ladoy P., Carbonnel J. P., Violette S., Desurosne, I. (1993). Multifractals and extreme rainfall events, Geophys. Res. Lett., 20(10), 931–934, 1993.

Kantelhardt J.W., Zschiegner S.A., Koscielny-Bunde E., Havlin S., Bunde A., Stanley H.E. (2002): Multifractal detrended fluctuaction analysis of nonstationary time series. Physica A, 316, 87-114.

Kaplan J. K., Yorke J. A. (1979). Chaotic behaviour of multidimensional difference equations, in: Functional Difference Equations and Approximation of Fixed Points, edited by: Walter, H. O. and Peitgen, H. O., Springer Verlag, Berlin, 730, 204–227.

Lana X., Fernández Mills G., Burgueño A. (1995). Daily precipitation maxima in Catalonia (NE Spain): Expected values and their spatial distribution. Inter. J. Climatol., 15, 341-354.

Lana X., Burgueño A. (2000a): Some statistical characteristics of monthly and annual pluviometric irregularity for the Spanish Mediterranean Coast. Theor. Appl. Climatol., 65, 79-97.

Lana X., Burgueño A. (2000b). Statistical distribution and spectral analysis of rainfall anomalies for Barcelona (NE Spain). Theor. Appl. Climatol., 66, 211-227.

Lana X., Serra C., Burgueño A. (2001). Patterns of monthly rainfall shortage and excess in terms of the Standardized Precipitation Index for Catalonia (NE Spain). Int. J. Climatol., 21, 1669-1691.

Lana X., Serra C., Burgueño A. (2003). Trends affecting pluviometric indices at the Fabra Observatory (Barcelona, NE Spain) from 1917 to 1999. Int. J. Climatol., 23, 315-332.

Lana X., Martínez M.D., Serra C., Burgueño A. (2005). Periodicities and irregularities of indices describing the daily pluviometric regime of the Fabra Observatory (NE Spain) for the years 1917-1999. Theor. Appl. Climatol., 82, 183-198.

Lana X., Burgueño A., Martínez M.D., Serra C. (2006). Statistical distributions and samplig strategies for the analysis of extreme dry spells in Catalonia (NE Spain). Journal of Hydrology, 324, 94-114.

Lana X., Martínez M.D., Burgueño A., Serra C. (2008a). Return period maps of dry spells for Catalonia (Northeastern Spain) based on the Weibull distribution. Hydrological Sciences, 53, 48-64.

Lana X., Martínez M.D., Burgueño A., Serra C., Martín-Vide J., Gómez L. (2008b): Spatial and temporal patterns of dry spell lengths in the Iberian Peninsula for the second half of the twentieth century. Theor. Appl. Climatol., 91, 99-116.

Lana X., Martínez M.D., Serra C., Burgueño A. (2010): Complex behaviour and predictability of the European dry spell regimes. Nonlin. Processes Geophys., 17, 499-512.

Lana X., Burgueño A., Martínez M.D., Serra C. (2012). Some characteristics of a daily rainfall regime based on the Dry Day Since Last Rain index (DDSLR). Theor. Appl. Climatol, 109, 153-174.

Lana X., Burgueño A., Serra C., Martínez, M.D. (2015). Complexity and predictability of the Western Mediterranean Oscillation index. Int. J. Climatol. DOI 10.1002/joc.4503.

de Lima M. I. P., Grasman J. (1999). Multifractal analysis of 15-min and daily rainfall from a semi-arid region in Portugal, J. Hydrol., 220, 1–11.

de Lima M. I. P., de Lima J. L. M. P. (2009). Investigating the multifractality of point precipitation in the Madeira archipelago. Nonlin. Processes Geophys., 16, 299–311.

López-Bustins J.A., Martín-Vide J., Sánchez-Lorenzo A. (2008): Iberia winter rainfall trends based upon changes in teleconnections and circulation patterns. Global and Planetary Change, 63, 171-176.

Lovejoy S., Mandelbrot B. B. (1985). Fractal properties of rain and a fractal model, Tellus, 37A, 209–232.

Malamud B.D., Turcotte D.L. (1999). Self-affine time series: Generation and analyses. Advances in Geophysics, 40, 1-90.

Mali P. (2015). Multifractal characterization of global temperature anomalies. Theor. Appl. Climatol.,121, 641-648. DOI 10.1007/s00704-014-1268-y.

Mandapaka P. V., Qin X. (2015). A large sample investigation of temporal scale-invariance in rainfall over the tropical urban island of Singapore. Theor. Appl. Climatol., 122, 685-697. DOI 10.1007/s00704-014-1317-6.

Mandelbrot BB, van Ness JW. (1968). Fractional Brownian motions, fractional noises and applications. SLAM Rev, 10, 422.

Martín-Vide J., López-Bustins J.A. (2006). The Western Mediterranean Oscillation and rainfall in the Iberian Peninsula. Int. J. Climatol., 26, 1455-1475.

Martín-Vide J., Sánchez-Lorenzo A., López-Bustins J.A., Cordobilla M.J., Garcia-Manuel A., Raso J.M. (2008). Torrential rainfall in northeast of the Iberian Peninsula: synoptic patterns and WeMO influence. Adv. Sci. Res., 2, 99-105.

Martínez M.D., Lana X., Burgueño A., Serra C. (2007a). Spatial and temporal daily rainfall regime in Catalonia (NE Spain) derived from four precipitation indices, years 1950-2000. Int. J. Climatol., 27, 123-138.

Martínez M.D., Lana X., Burgueño A., Serra C. (2007b). Lacunarity, predictability and predictive instability of the daily pluviometric regime in the Iberian Peninsula. Nonlin. Processes Geophys., 14, 109-121.

Martínez M.D., Lana X., Burgueño A. (2010). Long-term rainfall monthly shortage in Spain: spatial patterns, statistical models and time trends. Int. J. Climatol., 30, 1668-1688.

Martínez M.D., Lana X., Burgueño A., Serra C. (2012). Normalised monthly shortage curves: a contribution for a better understanding of monthly rain deficit in Western Europe. Theor. Appl. Climatol., 108, 535-552.

Mazzarella A. (1999). Multifractal dynamic rainfall processes in Italy. Theor. Appl. Climatol., 63, 73–78.

Mazzarella A., Tranfaglia, G. (2000). Fractal characterisation of geophysical measuring networks and its implication for an optimal location of additional stations: an application to a rain-gauge network. Theor. Appl. Climatol., 65, 157–163.

Olsson J., Niemczynowicz J., Berndtsson, R.(1993). Fractal analysis of high-resolution rainfall time series, J. Geophys. Res., 98, 23 265–23 274.

Ouachani R., Bargaoui Z., Ouarda T. (2013). Power of teleconnection patterns on precipitation and extreme flow variability of upper Medjerda Basin. Int. J. Climatol., 33, 58-76.

Palutikof J. (2003). Analysis of Mediterranean climate data: measured and modelled. In Mediterranean Climate: Variability and Trends, Bolle HJ (ed). Springer-Verlag: Berlin.

Pan Chun K., Wheater H., Onof C. (2013). Prediction of the impact of climate change on drought: an evaluation of six UK catchments using two stochastic approaches. Hydrol. Process. 27, 1600–1614.

Press W.H., Teukolsky S.A., Vetterling W.T., Flannery B.P. (1992). Numerical recipes in FORTRAN, 2ed. Cambridge University press, Cambridge.

Ríos-Cornejo D., Penas A., Álvarez-Esteban R., del Río S. (2015a). Links between teleconnection patterns and precipitation in Spain. Atmospheric Research, 156, 14–28.

Ríos-Cornejo D., Penas A., Álvarez-Esteban R., Del Río S. (2015b). Links between teleconnection patterns and mean temperature in Spain. Theor. Appl. Climatol., DOI 10.1007/s00704-014-1256-2.

Rodríguez R., Casas M. C., Redaño A. (2013): Multifractal analysis of the rainfall time distribution on the metropolitan area of Barcelona (Spain). Meteorol. Atmos. Phys., 121, 181-187. DOI 10.1007/s00703-013-0256-6.

Rodríguez-Iturbe I., Febres de Power B., Sharifi M. B., Georgakakos K. P. (1989). Chaos in rainfall, Water Resour. Res., 25, 1667–1675.

Salas J. D., Kim S. H., Eykholt R., Burlando P., Green T.R. (2005). Aggregation and sampling in deterministic chaos: implication for chaos identification in hydrological processes, Nonlin. Processes Geophys., 12, 557–567.

Sánchez-Lorenzo A., Calbó J., Brunetti M., Deser C. (2009) : Dimming/brightening over the Iberian Peninsula: trends in sunshine duration and cloud cover and their relation with atmospheric circulation. J. Geophys. Res., 114, D00D09.

Serra C. (1994). Análisis en componentes principales y algoritmos de clasificación automática. Aplicación al estudio del comportamiento de la precipitación en Catalunya y a la obtención local de tipos de tiempo. PhD Thesis. Universidad de Barcelona. 448 pp.

Serra, C., Fernández Mills, Periago, M.C. and X. Lana. (1996). Winter and autumn daily precipitation patterns in Catalonia, Spain. Theor. Appl. Climatol., 54(3-4), 175-186.

Serra C., Burgueño A., Martínez M.D., Lana X. (2006). Trends in dry spells across Catalonia (NE Spain) during the second half of the 20th century. Theor. Appl. Climatol., 85, 165-183.

Serra C., Martínez M.D., Lana X., Burgueño A. (2013). European dry spell length distributions, years 1951-2000. Theor. Appl. Climatol., 114, 531-551

Serra C., Martínez M.D., Lana X., Burgueño A. (2014). European dry spell regimes (1951-2000): Clustering process and time trends. Atmospheric Res., 144, 151-174.

Shimizu Y., Thurner S., Ehrenberger K. (2002): Multifractal spectra as a measure of complexity in human posture. Fractals, 10, 103-116.

Sivakumar B. (2001a). Rainfall dynamics at different temporal scales: A chaotic perspective. Hydrol. Earth Syst. Sci., 5, 645–651.

Sivakumar, B. (2001b). Is a chaotic multi-fractal approach for rainfall possible? Hydrol. Processes, 15, 943–955.

Sivakumar B., Sorooshian S., Gupta H. V., Gao X. (2001). A chaotic approach to rainfall disaggregation, Water Resour. Res., 37, 61–72.

Stephenson D.B., Pavan V., Bojariu R. (2000). Is the North Atlantic Oscillation a random walk? Int. J. Climatol., 20, 1-18.

Stoop F., Meier P. F.(1988). Evaluation of Lyapunov exponents and scaling functions from time series, J. Opt. Soc. Am. B, 5, 1037–1045.

Svensson C., Olsson J., Berndtsson R. (1996). Multifractal properties of daily rainfall in two different climates, Water Resour. Res., 32, 2463–2472.

Tessier Y., Lovejoy S., Hubert P., Shertzer D., Pecknold S. (1996). Multifractal analysis and modelling of rainfall and river flows and scaling, causal transfer functions, J. Geophys. Res., 101, 26 427–26 440.

Triacca U., Pasini A., Attanasio A. (2014). Measuring persistence in time series of temperature anomalies. Theor. Appl. Climatol. , 118, 491-495. DOI 10.1007/s00704-013-1076-9.

Turcotte D.L. (1997). Fractals and Chaos in Geology and Geophysics (2nd Edition). Cambridge University Press, Cambridge, UK, 398 pp.

Valencia J. L. , Saa Requejo A., Gascó J. M., Tarquis A. M. (2010). A universal multifractal description applied to precipitation patterns of the Ebro River Basin, Spain. Clim. Res., 44, 17–25.

Veneziano D., Bras R. L., Niemann J. D. (1996). Nonlinearity and self-similarity of rainfall in time and a stochastic model, J. Geophys. Res., 101, 26 371–26 392.

Verrier S., Mallet C., Barthès L. (2011). Multiscaling properties of rain in the time domain, taking into account rain support biases. J. Geophys. Res., 116, D20119.

Vicente-Serrano S.M., Beguería S., López-Moreno J.I., El Kenawy A.M., Angulo-Martínez M. (2009). Daily atmospheric circulation events and extreme precipitation risk in northeast Spain: Role of the North Atlantic Oscillation, the Western Mediterranean Oscillation, and the Mediterranean Oscillation. J. Geophys. Res., 114(D8), DOI: 10.1029/2008JD011492.

Wang H. R., Wang C., Lin X., Kang J. (2014). An improved ARIMA model for precipitation simulations. Nonlin. Processes Geophys., 21, 1159–1168.

Wiggins S. (2003). Introduction to applied nonlinear dynamical systems and chaos (2nd edition). Text in Applied Mathematics, 2. Springer, New York, 843 pp.

Yonghe L., Kexin Z., Wanchang Z., Yuehong S., Hongqin P., Jinming F.(2013). Multifractal analysis of 1-min summer rainfall time series from a monsoonal watershed in eastern China. Theor. Appl. Climatol.,111, 37-50. DOI 10.1007/s00704-012-0627-9.

Yonghe L., Wanchang Z., Kexin Z., Hongqin P.(2012). Multifractal analysis of daily rainfall from a monsoon watershed in Eastern China. Theor. Appl. Climatol., 107, 591-598. DOI 10.1007/s00704-011-0505-x.

List of Figures

Figure 1. MRA time series recorded at Fabra Observatory since 1917 to 2010 at a) monthly scale and b) along spring, summer, autumn and winter seasons**.**

Figure 2. Time series of the WeMOi at (a) monthly scale and (b) for spring, summer, autumn and winter seasons.

Figure 3. MRA monofractal analysis. a) Hurst. b) Hausdorff exponents, where black points are the selected values for an optimum log-log regression in agreement with Malamud and Turcotte (1999). c) correlation integral and d) correlation dimension.

Figure 4. a) Kolmogorov entropy and b) the two first Lyapunov exponents (λ_1 = 0.16 and λ_2 = 0.11) deduced from the reconstruction theorem.

Figure 5. MRA multifractal analysis based on the MF-DFA. a) Examples of *q*-order fluctuation function, $F_q(s)$, as a function of segment length s and for *q*=±15. b) Dependence of the generalised Hurst exponent, h(q), on *q*. c) and d) Evolution of the Hölder exponent, α_0, and $\tau(q)$ on *q*. e) Multifractal spectrum, shown by the open circles and centred on the critical Hölder exponent, α_0, and its second degree polynomial fit (solid line). Straight dashed line depicts the theoretical upper limit of the multifractal spectrum.

Figure 6. a) Auto-correlation and b) power spectrum of MRA recorded at the Fabra Observatory. c) Comparison between MRA and fGn.

Figure 7. Results of the AR(p) process for MRA. a) Evolution of MAD with the autoregressive order, *p*. b) Time series of the MRA residuals. c) Histogram of the MRA residuals.

Figure 8. MRA regressive prediction by assuming dependence on WeMOi. a) Evolution of MAD with the autoregressive order, *p*. b) Time series of the MRA residuals. c) Histogram of the MRA residuals. d) Relationship between MRA residuals and WeMOi.

Figure 9. (a) Spring, summer, autumn and winter cross-correlations, (b) monthly cross-correlation and (c) cross-power spectrum for MRA and WeMOi.

Figure 10. Relationship between MRA and WeMOi for a) the whole recording period and b) spring, summer, autumn and winter seasons.

Figure 11. a) Evolution of the percentage of positive WeMOi with increasing MRA. b) Average WeMOi, <WeMO>, for different MRA intervals of 15 mm/month.

	Monofractal parameters							*MF-DFA*		
	H	H_a	β	μ^*	κ	λ_1	D_{KY}	α_0	B	W
MRA	0.54	0.01	−0.04	7.18	1.09	0.16	13.10	0.52	−1.08	0.44
WeMOi	0.67	0.05	0.17	9.68	0.64	0.16	12.43	0.57	1.01	0.23

Table 1. Summary of monofractal and multifractal parameters of MRA (this research) and WeMOi (Lana et al., 2015).

	fGn	**ARIMA$_{MRA}$**	**ARIMA$_{WeMOi}$**
MAD (mm/month)	61.6	47.1	46.0
σ_{res} (mm/month)	55.6	45.1	40.4
$\sigma_{res}/\sigma_{MRA}$	1.15	0.93	0.83

Table 2. Summary of MAD, standard deviations of MRA residuals, σ_{res}, and the ratio $\sigma_{res}/\sigma_{MRA}$, where the standard deviation of MRA, σ_{MRA} , is 48.4 mm/month, for the three applied predictive processes.

Month	**WeMOi**	**MRA**	**ndW+**	**ndW-**	**ndW0**	**nrd**	**Rmax**	**<R>**	**σ(R)**
October 1965	-3.21	285.3	0	27	4	16	50.0	17.8	17.1
December 1971	-0.99	365.6	6	13	12	12	196.0	30.5	55.8
September 1993	1.00	248.1	12	6	12	7	90.9	35.4	31.6

Table 3. Three selected months with different WeMOi signs and high MRA (mm/month). The number of days with positive, negative and almost null daily WeMO index are designed by ndW+, ndW- and ndW0 respectively. nrd is the number of rainfall days, Rmax the maximum daily rainfall (mm/day) and <R> and σ(R) the average and standard deviation (mm/day) of daily rainfall amounts.

a)

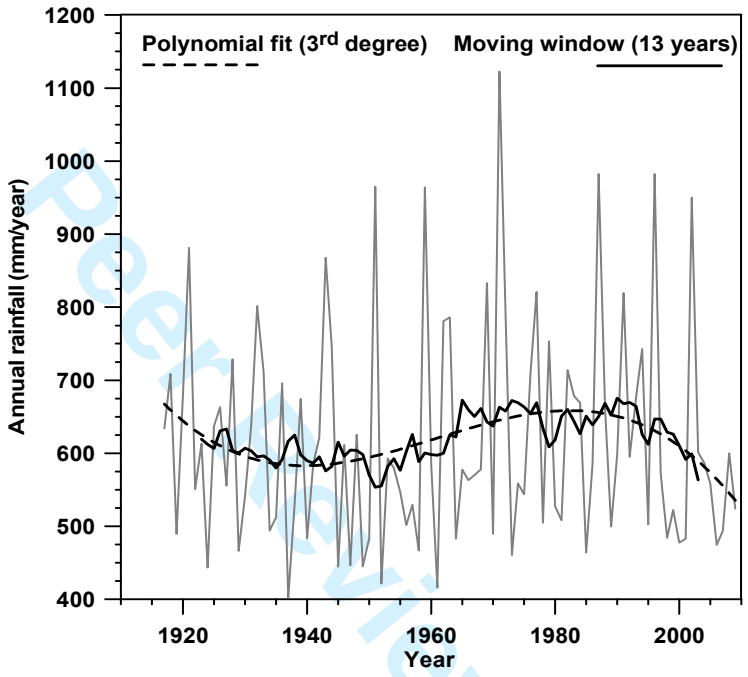

b)

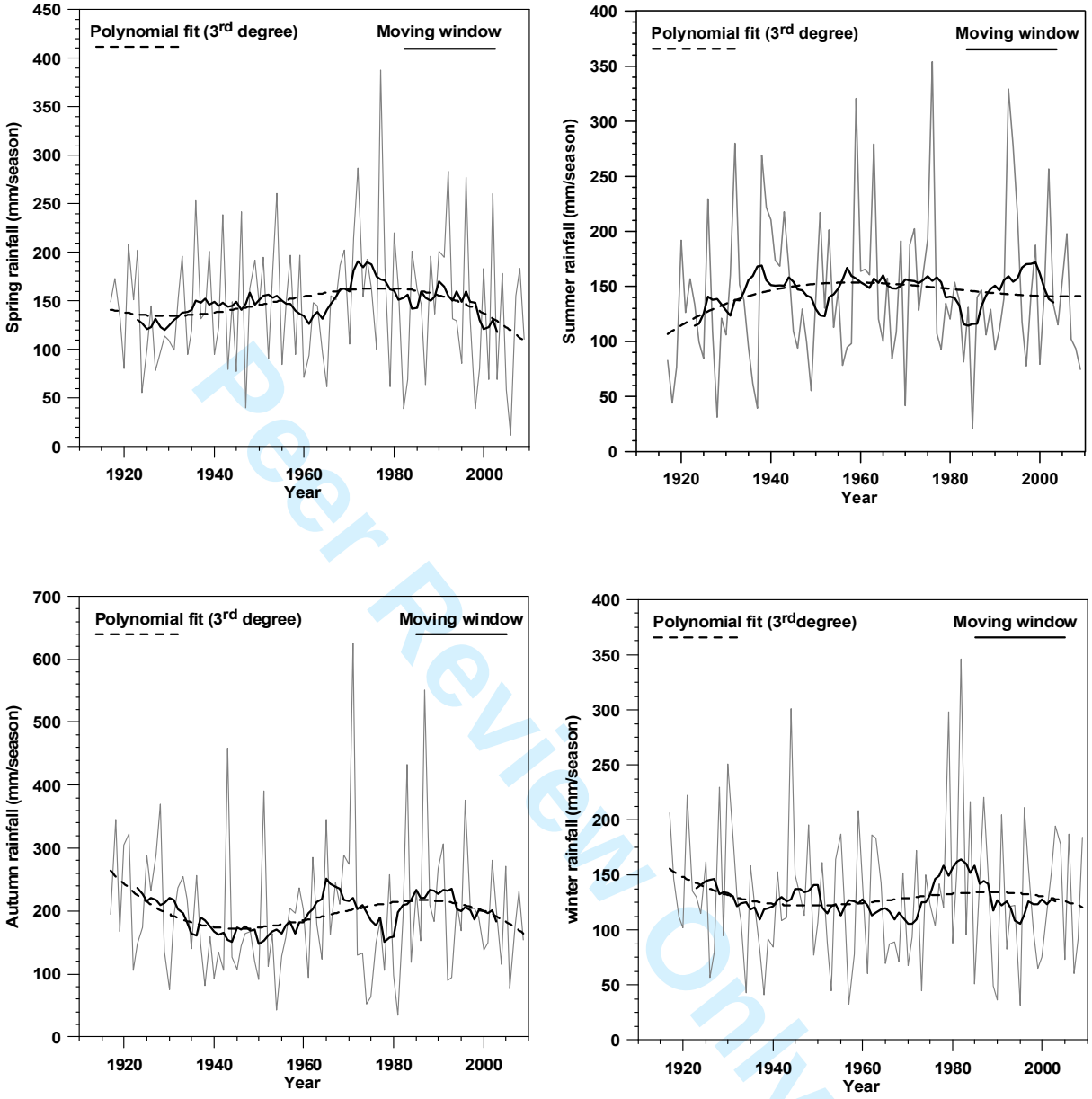

Figure 1

a)

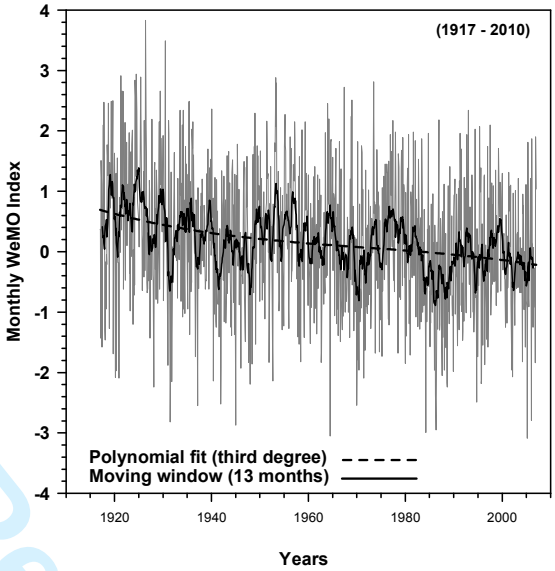

b)

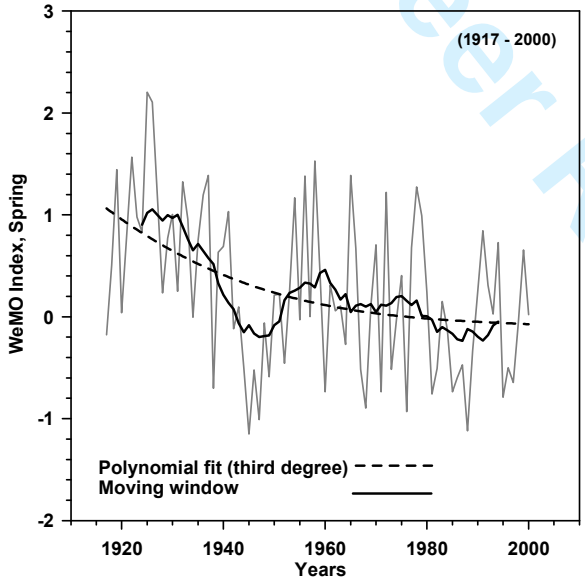

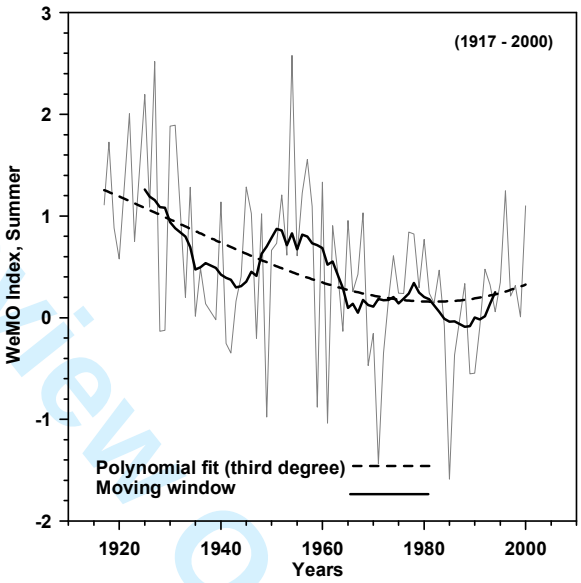

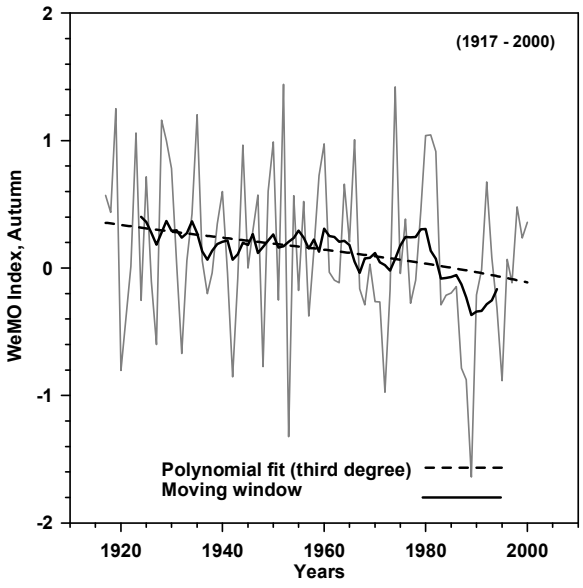

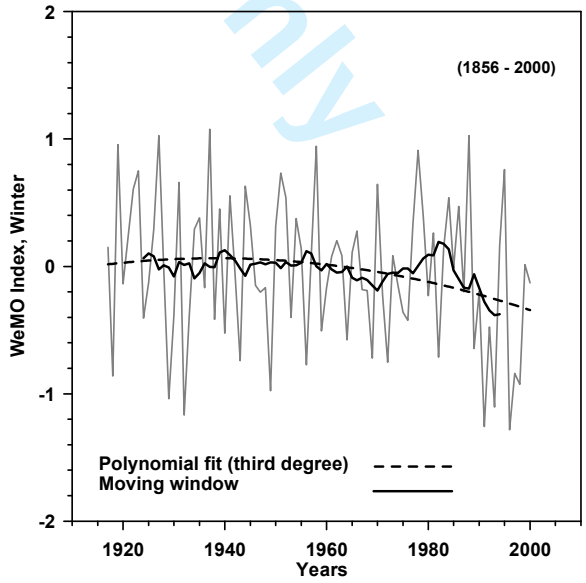

Figure 2

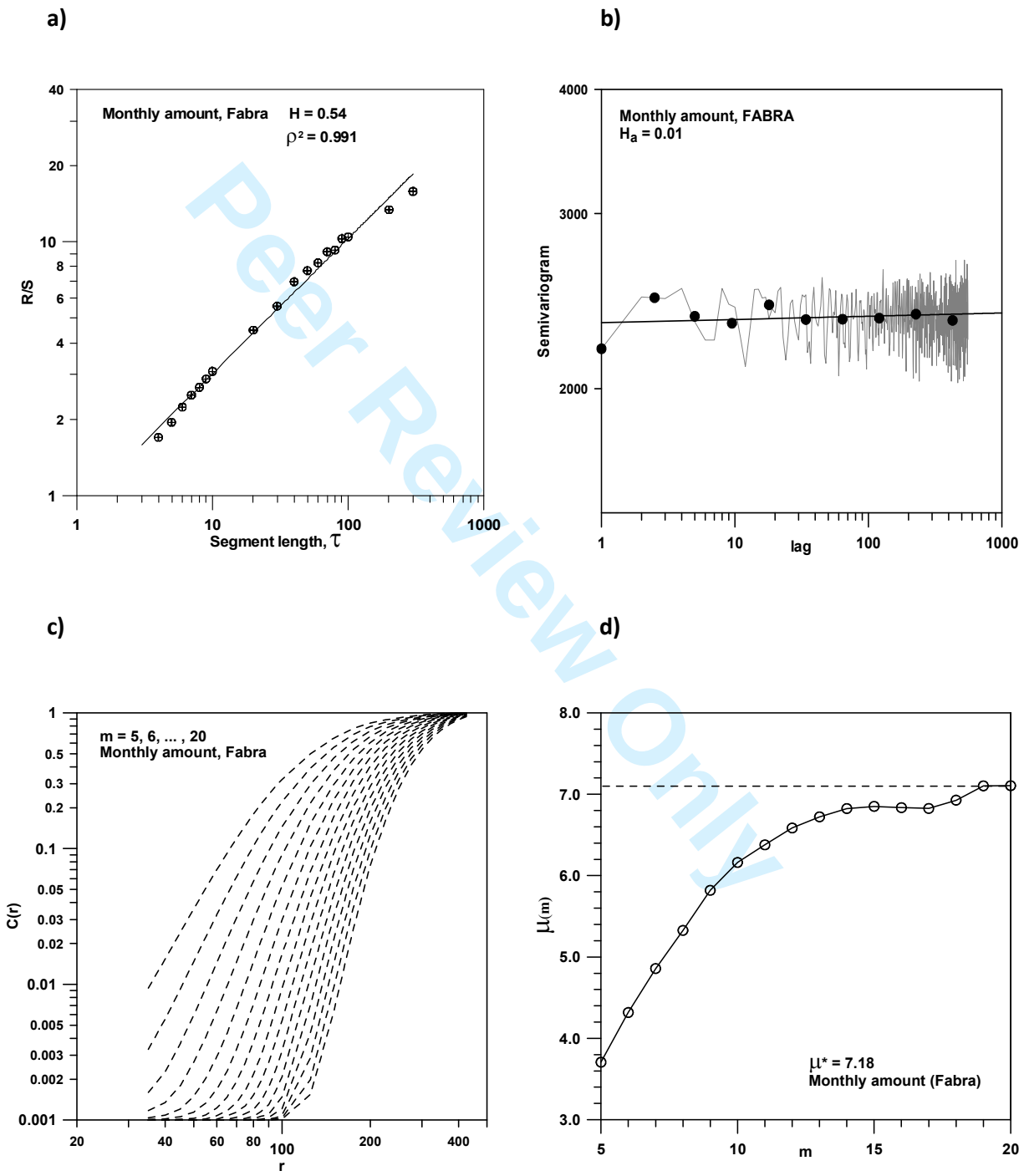

Figure 3

a)

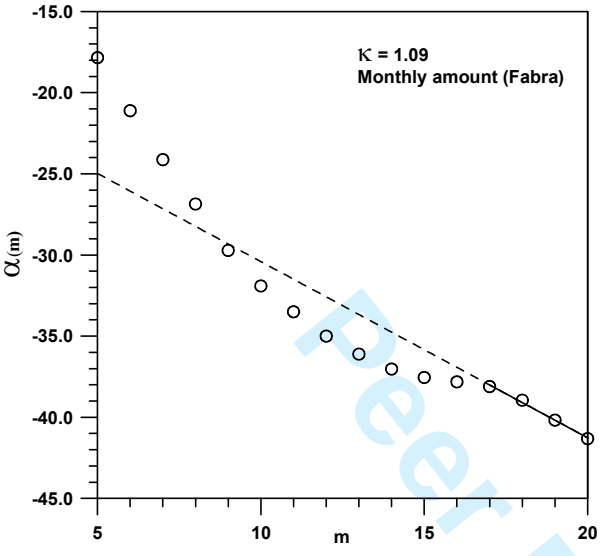

b)

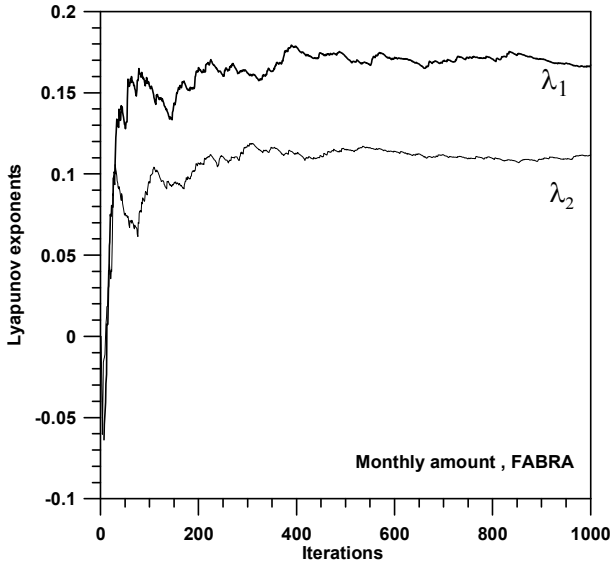

Figure 4

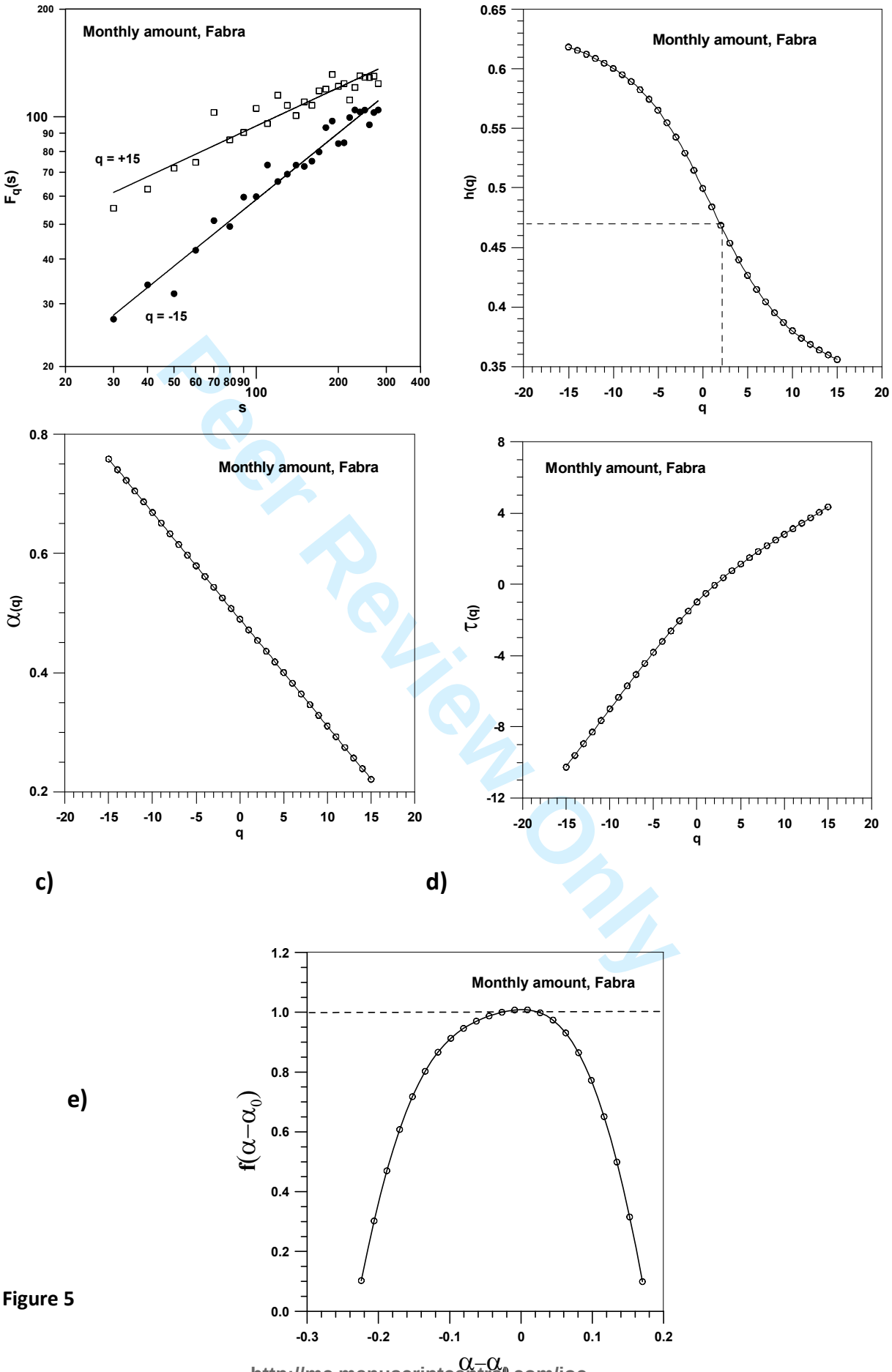

Figure 5

a)

b)

c)

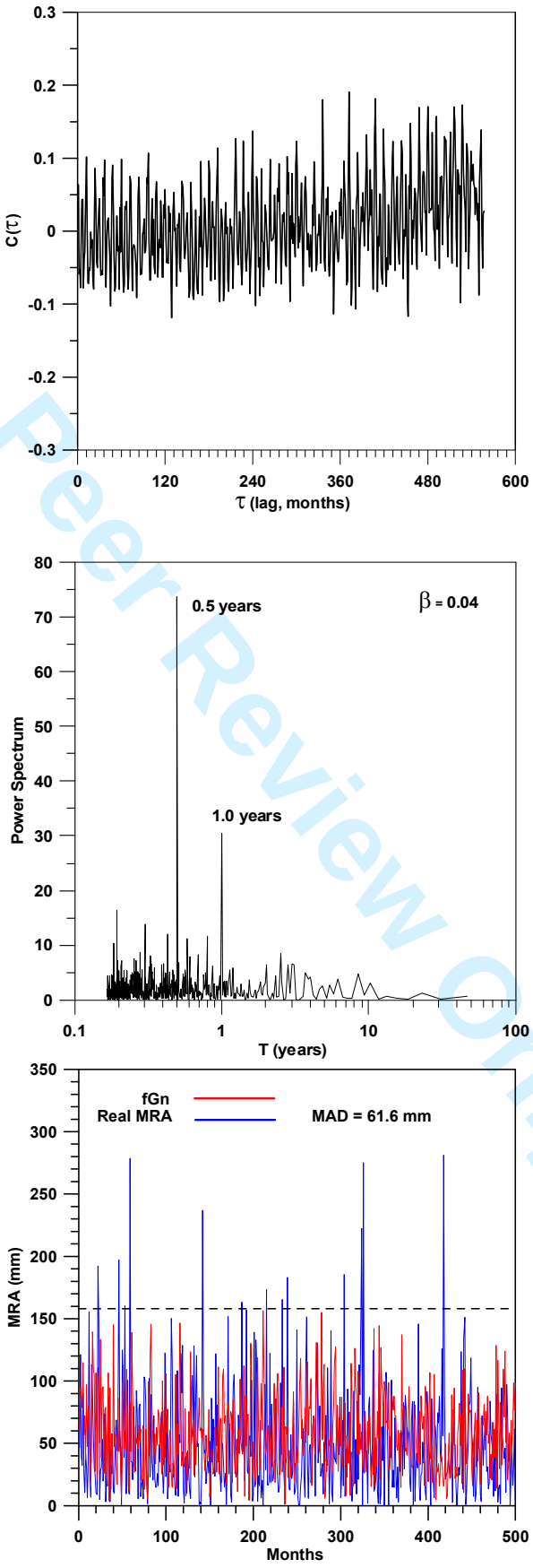

Figure 6

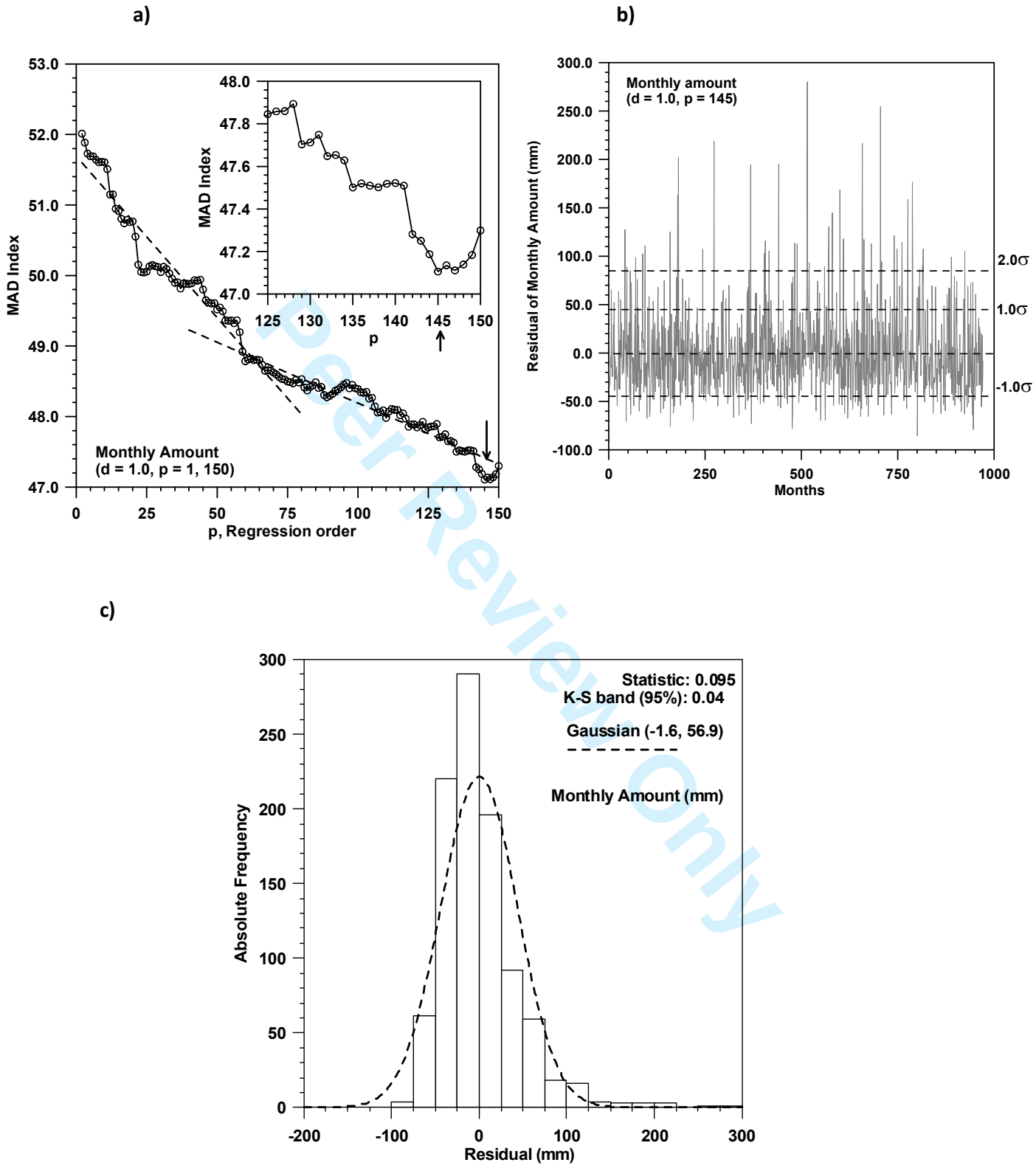

Figure 7

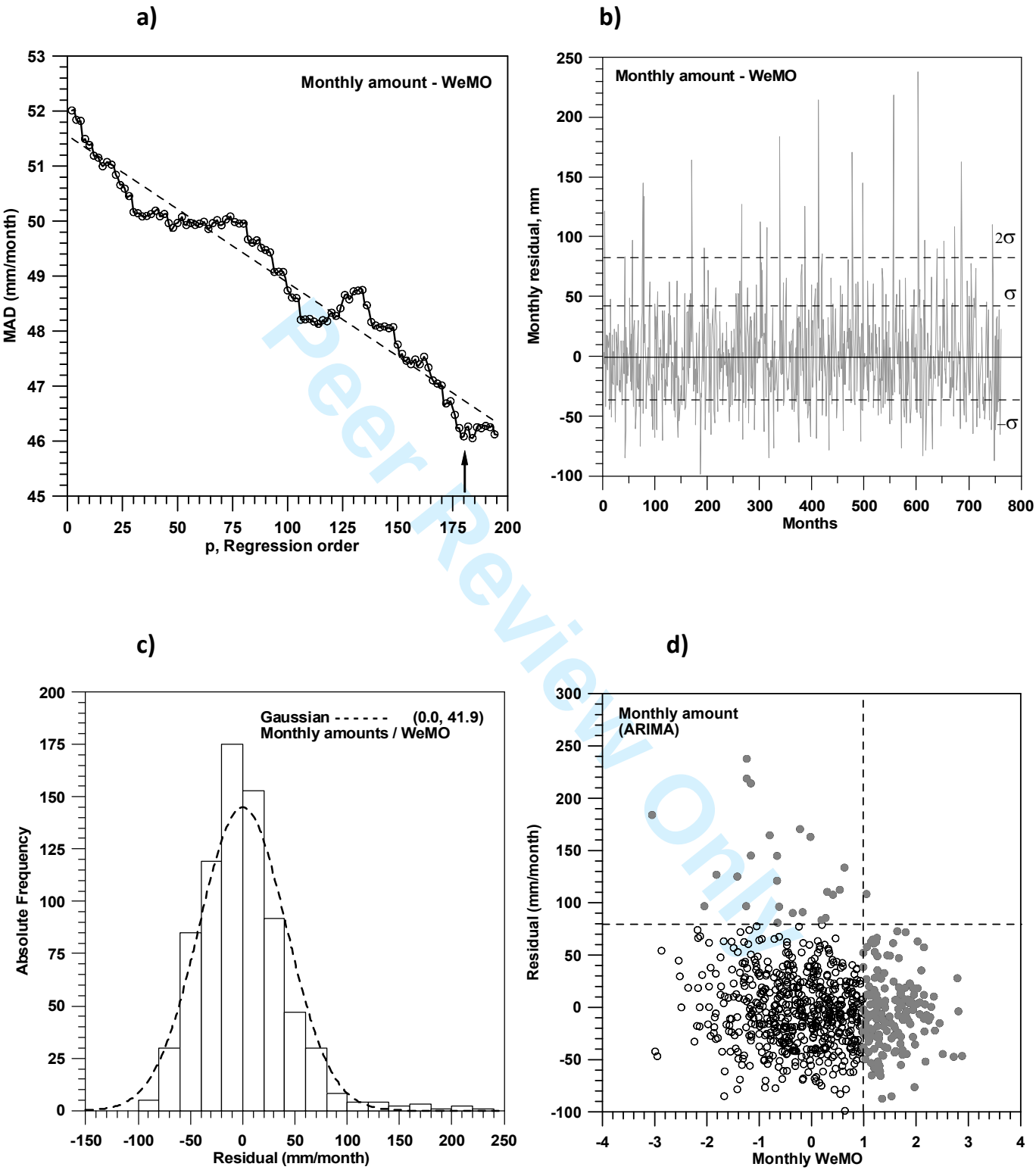

Figure 8

a)

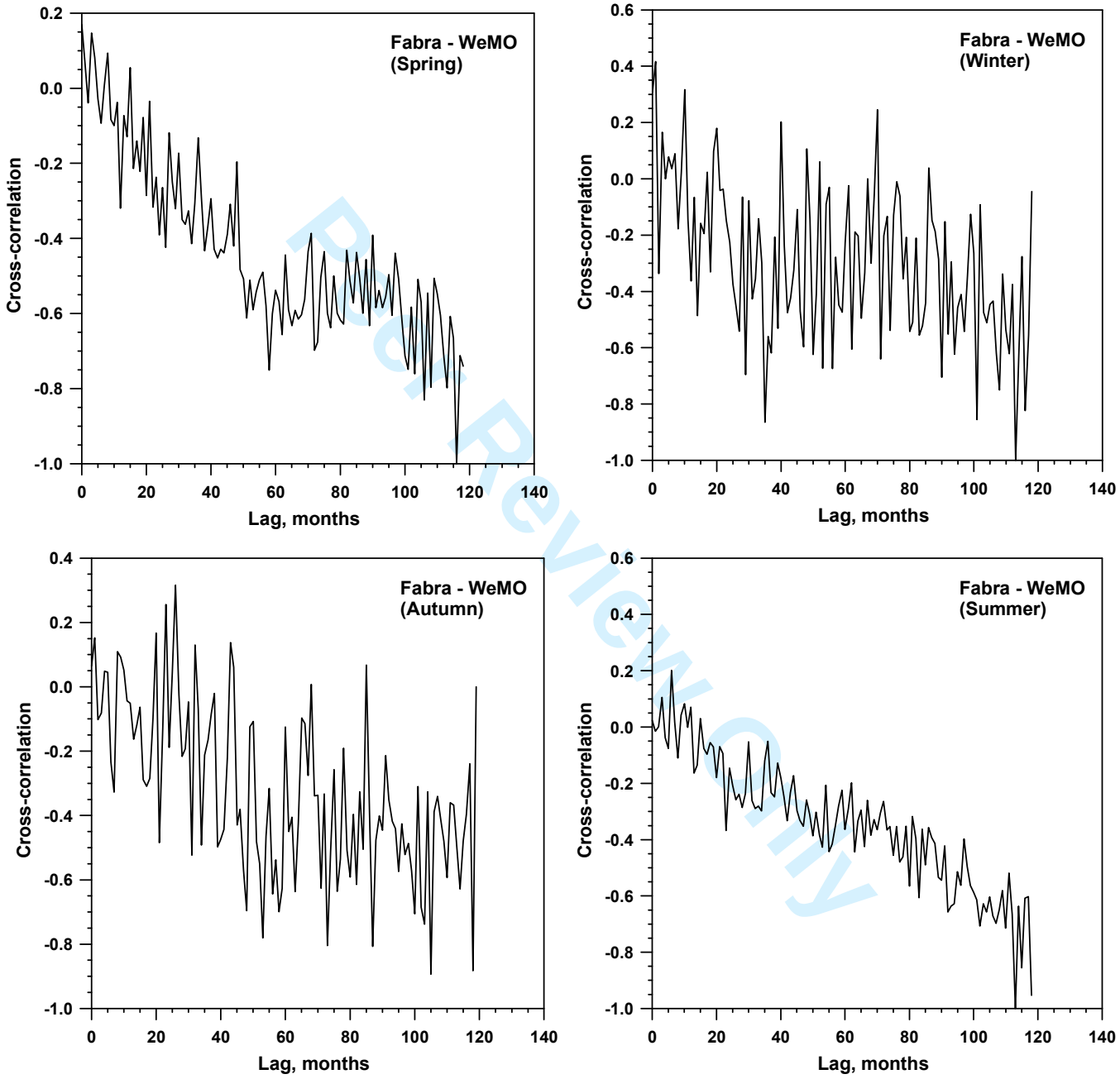

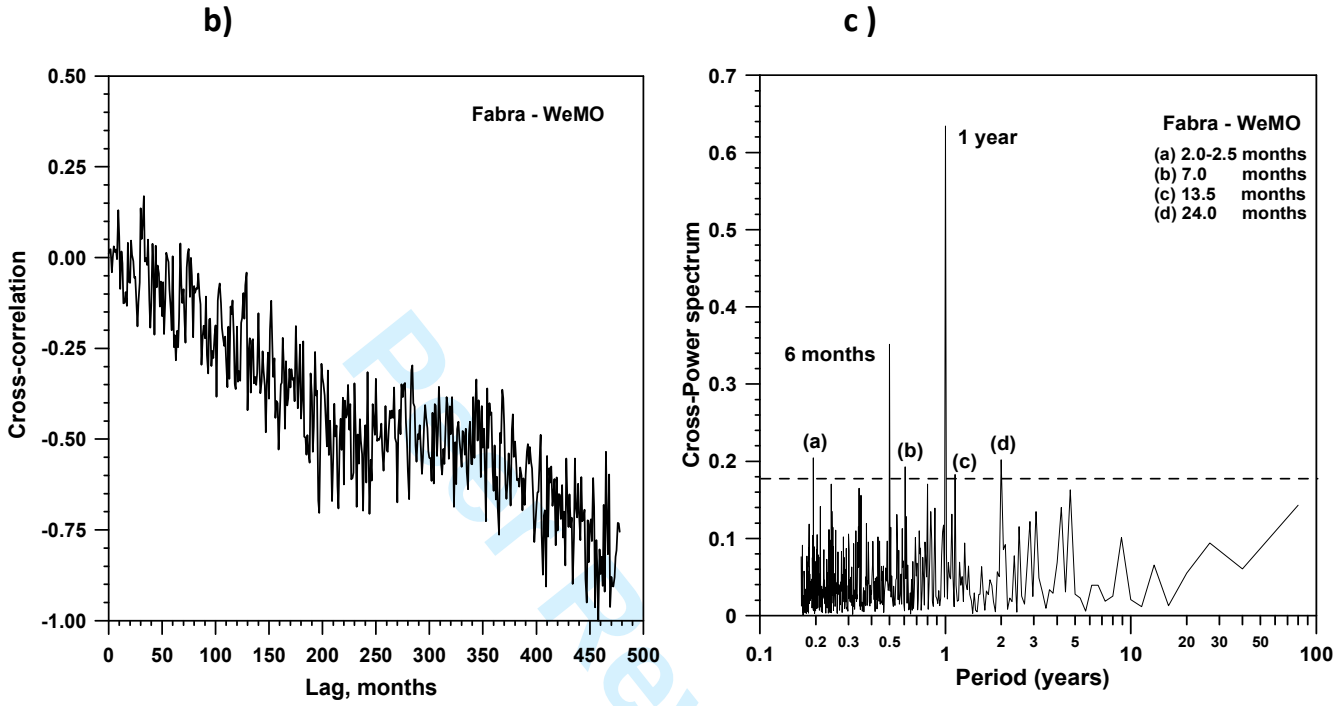

Figure 9

a)

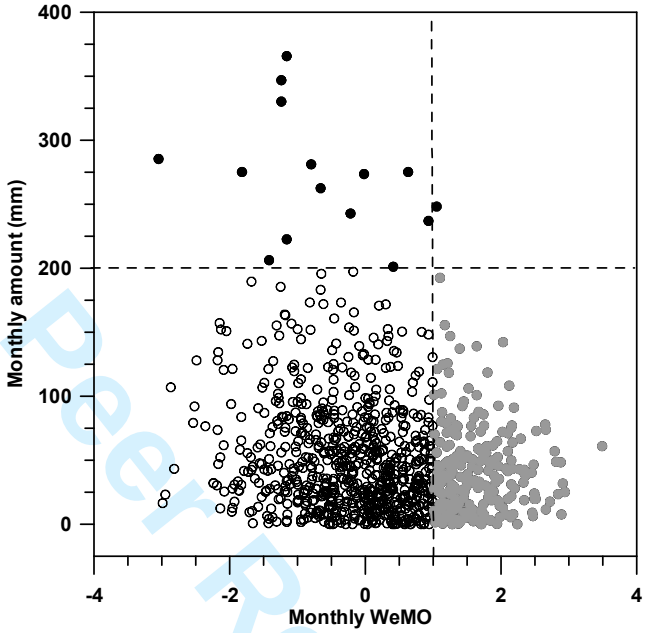

b)

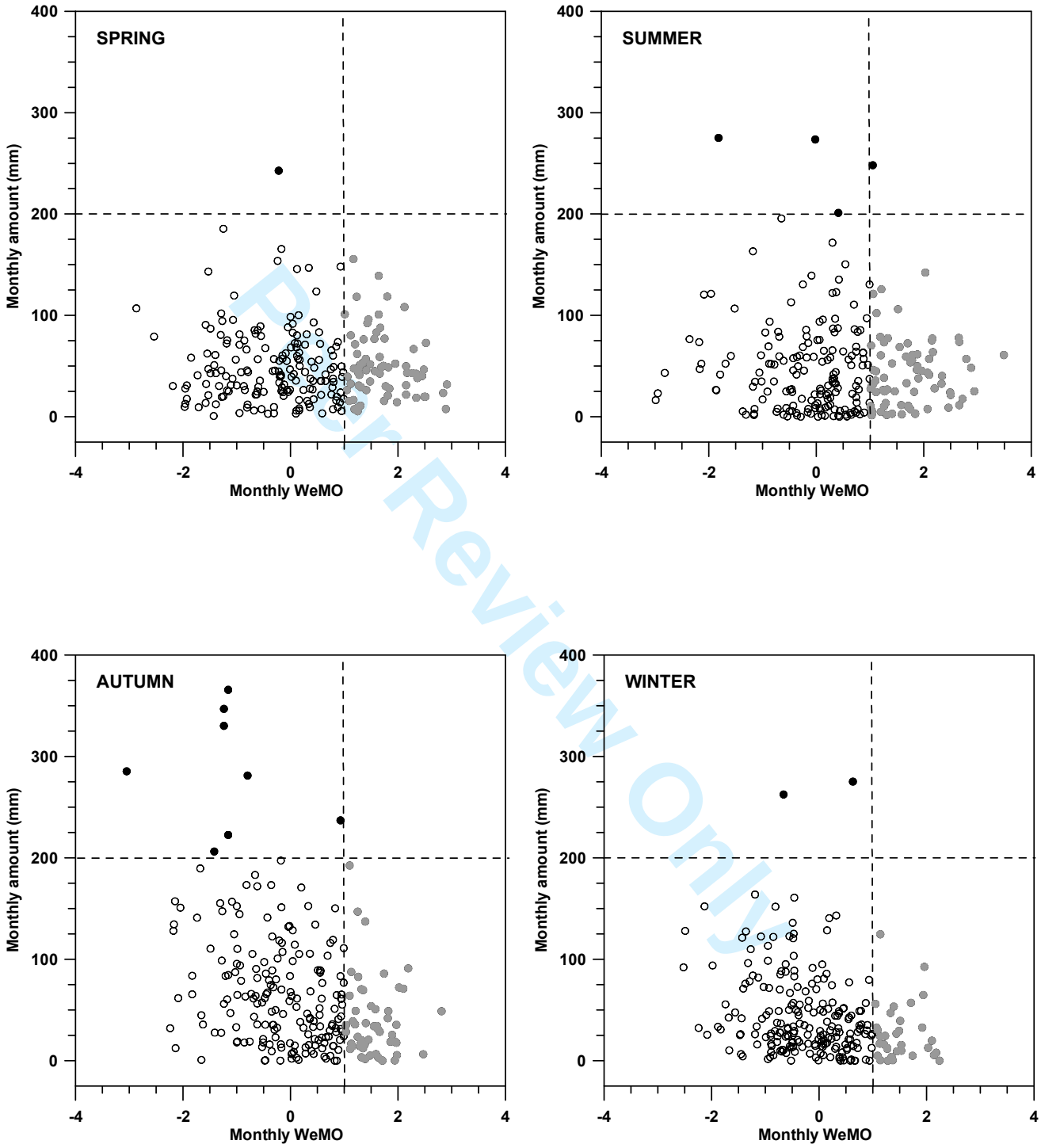

Figure 10

a)

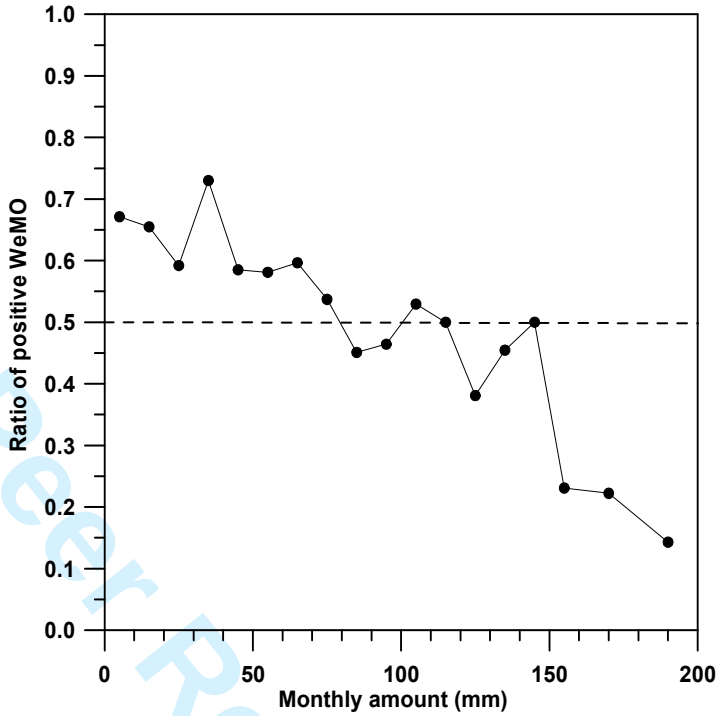

b)

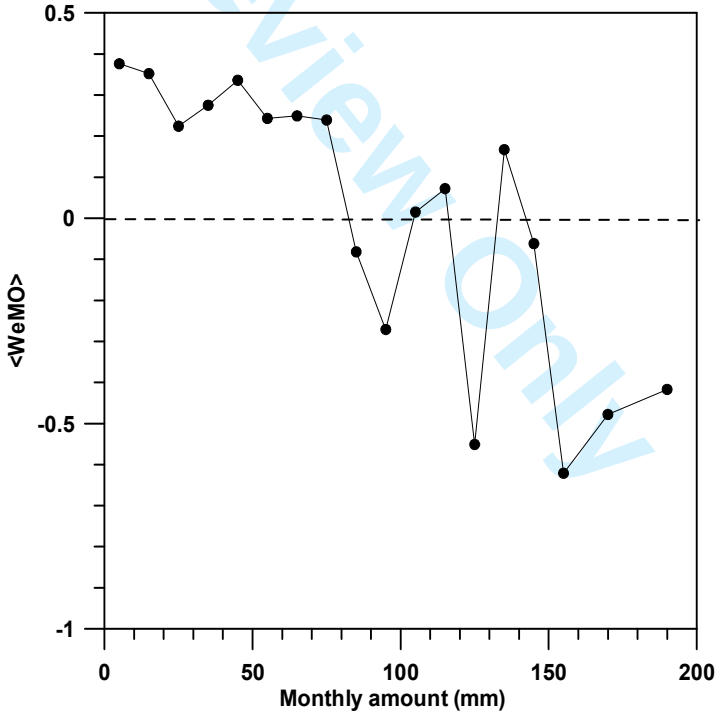

Figure 11